

# Shape curvature effects in viscous streaming

Yashraj Bhosale and Tejaswin Parthasarathy

*Mechanical Sciences and Engineering, University of Illinois at Urbana-Champaign, Urbana, IL 61801, USA*

Mattia Gazzola\*

*Mechanical Sciences and Engineering and National Center for Supercomputing Applications,  
University of Illinois at Urbana-Champaign, Urbana, IL 61801, USA*

Viscous streaming flows generated by objects of constant curvature (circular cylinders, infinite plates) have been well understood. Yet, characterization and understanding of such flows when multiple body length-scales are involved has not been looked into, in rigorous detail. We propose a simplified setting to understand and explore the effect of multiple body curvatures on streaming flows, analysing the system through the lens of bifurcation theory. Our setup consists of periodic, regular lattices of cylinders characterized by two distinct radii, so as to inject discrete curvatures into the system, which in turn affect the streaming field generated due to an oscillatory background flow. We demonstrate that our understanding based on this system can be then generalised to a variety of individual convex shapes presenting a spectrum of curvatures, explaining prior experimental and computational observations. Thus, this study illustrates a route towards the rational manipulation of viscous streaming flow topology, through regulated variation of object geometry.

## I. Introduction

This paper investigates the role of body curvature in two-dimensional viscous streaming phenomena. Viscous streaming refers to the time-averaged steady flow that arises when an immersed body of characteristic length scale  $D$  undergoes small-amplitude oscillations (compared to  $D$ ) in a viscous fluid. Viscous streaming has been well explored and characterized theoretically, experimentally and computationally, for constant curvature shapes which include oscillating individual circular cylinders [1–5], infinite flat plates [6, 7] and spheres [8–10]. However, little is known beyond these simple objects, in particular when multiple curvatures in complex shapes are involved. Efforts have been made in this direction by considering individual oscillating ellipses [11], spheroids [10], triangle and square cylinders [12, 13], sharp edges [14, 15] as well as multiple identical cylinders [4, 16, 17]. Yet, our understanding of how streaming flow features and topology are affected by multiple body length scales remains largely incomplete.

Our motivation to understand these relations stems from the broad range of applications of viscous streaming in microfluidic flow manipulation, particle trapping, scalar transport and passive swimming [18–28] which can benefit from an expanded flow design space based on geometrical variations. Additionally, we are motivated by the emergence of artificial and biohybrid mini-bots operating in fluids [29–33]. Indeed, these bots operate across flow regimes where streaming effects can be important, and may be usefully leveraged, opening new opportunities for micro-robotics in manufacturing or medicine [31]. For example, in a recent study [34], we showed that streaming can enhance the contactless transport of passive inertial particles (drug payload) by moving cylindrical mini-bots. There, we also highlighted that morphing a circular cylinder to a suitably sculpted shape that combines asymmetry and high rear curvature, can further improve transport. We attributed this enhancement to a favourable re-arrangement of the streaming flow topology. This raises the question—how do changes in geometry from a circular cylinder translate into streaming flow topology organization? Can we rigorously predict and manipulate topological transitions

---

\*Electronic address: mgazzola@illinois.edu

through shape variations for flow design purposes?

In this work, we attempt to answer these questions by first understanding and characterizing streaming flow topology in a simplified setting in which circular cylinders of different radii (i.e. curvatures) are arranged in periodic, regular lattices. This allows us to inject multiple curvatures in a discrete fashion into our system, enabling a systematic study of their effects. We analyse the different flow topologies that arise as we vary the cylinders' curvature ratios and the frequency of the background oscillatory flow, and characterize their transitions via bifurcation theory. Finally, we demonstrate that our understanding can be extended to generalised, individual bodies, aided by comparison against prior experiments [12, 13] and computations [34]. Overall, this study elucidates the mechanisms at play when streaming flow topology is manipulated via regulated variations of shape geometry, thus providing a rational design approach and physical intuition.

The work is organized as follows: governing equations and numerical method are recapped in §II; streaming physics is described in §III; lattice setup, investigation of different flow topologies and corresponding transitions are presented in §IV; extension to the design of arbitrary geometries and comparison against experiments is discussed in §V; finally, our findings are summarized and discussed in §VI.

## II. Governing equations and numerical method

We briefly recap the governing equations and the numerical solution technique. We consider incompressible viscous flows in a periodic or unbounded domain  $\Sigma$ . In this fluid domain, immersed solid bodies perform simple harmonic oscillations. The bodies are density-matched and have support  $\Omega$  and boundary  $\partial\Omega$  respectively. The flow can then be described using the incompressible Navier–Stokes equations (1)

$$\nabla \cdot \mathbf{u} = 0; \quad \frac{\partial \mathbf{u}}{\partial t} + (\mathbf{u} \cdot \nabla) \mathbf{u} = -\frac{\nabla P}{\rho} + \nu \nabla^2 \mathbf{u}, \quad \mathbf{x} \in \Sigma \setminus \Omega \quad (1)$$

where  $\rho$ ,  $P$ ,  $\mathbf{u}$  and  $\nu$  are the fluid density, pressure, velocity and kinematic viscosity, respectively. The dynamics of the fluid–solid system are coupled via the no-slip boundary condition  $\mathbf{u} = \mathbf{u}_s$ , where  $\mathbf{u}_s$  is the solid body velocity. The system of equations is then solved using a velocity–vorticity formulation with a combination of remeshed vortex methods and Brinkmann penalization [35]. This method has been validated across a range of flow–structure interaction problems, from flow past bluff bodies to biological swimming [35–39]. Recently, it has also been shown to effectively capture spatio–temporal scales related to viscous streaming [34].

## III. Streaming: physics and flow topology

### A. Streaming physics: classical case of a circular cylinder

We first characterize streaming in the simple, classical setting of a circular cylinder undergoing oscillations. We consider a cylinder of constant curvature  $\kappa$  (radius  $r = 1/\kappa$ ), in quiescent flow, with an imposed small amplitude oscillatory motion  $x(t) = x(0) + A \sin(\omega t)$  where  $A$  and  $\omega$  are the dimensional amplitude and the angular frequency, respectively. These small amplitude oscillations ( $A\kappa \ll 1$ ) generate a Stokes layer of thickness  $\delta_{AC} \sim O(\sqrt{\nu/\omega})$  around the cylinder, also known as the AC boundary layer. The velocity that persists at the edge of this AC layer then drives a viscous streaming response in the surrounding fluid [40]. This streaming response is depicted in figure 1(a, b) as clockwise (blue) and anti-clockwise (orange) vortical flow structures around the cylinder. We characterize these flow structures using the streaming Reynolds number  $R_s = A^2\omega/\nu$  [2, 41]. Figure 1(a) shows a flow representative of  $R_s \ll 1$ . Such low  $R_s$  indicates dominant viscous effects, and indeed the steady streaming flow is Stokes-like, with characteristic slow velocity decay and recirculating regions extending practically to infinity. Figure 1(b) is representative of larger

$R_s \sim O(1) - O(10)$ , where the interplay of inertial and viscous effects leads to the formation of a well defined boundary layer of thickness  $\delta_{DC}$ , also known as the DC boundary layer, which drives the fluid in the bulk. The normalized DC layer thickness  $\delta_{DC}\kappa$  and the AC layer thickness  $\delta_{AC}\kappa$ , can be directly related as illustrated in figure 1(c) [3, 42]. Then, in the classical constant curvature setting of a single cylinder, specifying  $\delta_{AC}\kappa$  is sufficient to characterize the streaming flow field and its topology. This picture breaks down when more complex shapes are considered, and a more generic approach to characterize streaming flows becomes necessary.

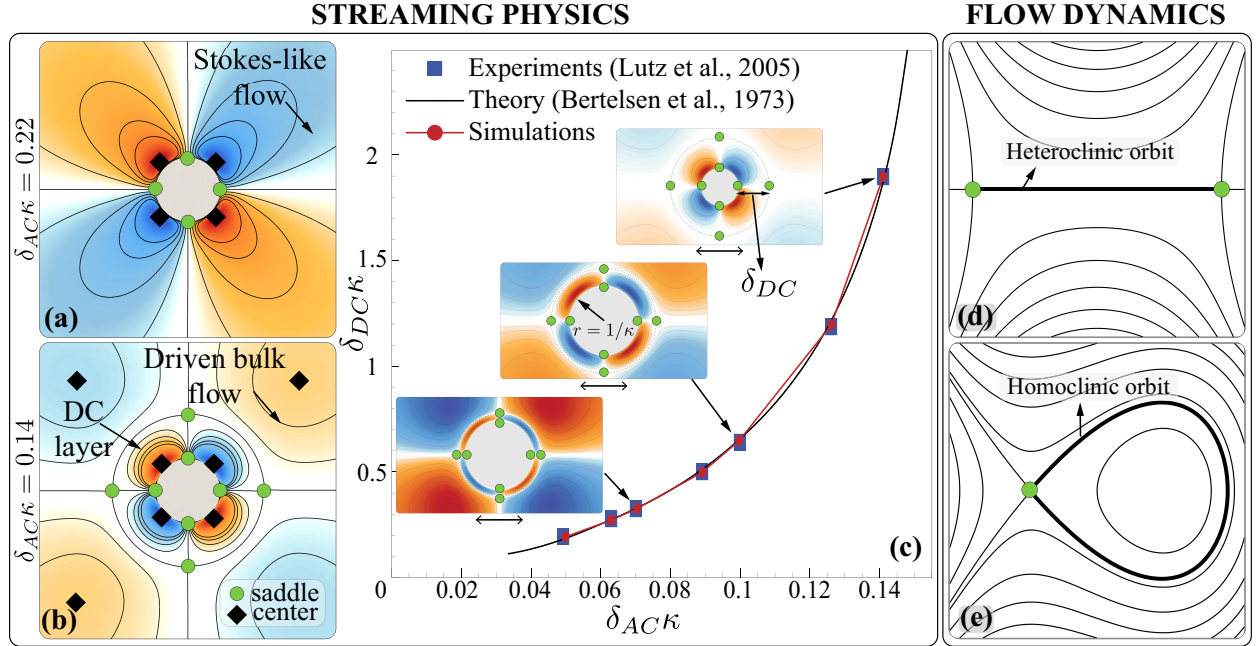


FIG. 1: Streaming characterization in classical circular cylinder setting. Comparison of time-averaged streamline patterns in (a) Stokes-like ( $\delta_{AC}\kappa = 0.22$ ) and (b) finite-thickness DC layer ( $\delta_{AC}\kappa = 0.14$ ) regimes, respectively, with the corresponding critical points. Centres and saddles (half-saddles on solid boundaries) are denoted as black diamonds and green circles, respectively. (c) Comparison of normalized DC boundary layer thickness  $\delta_{DC}\kappa$  vs. normalized AC boundary layer thickness  $\delta_{AC}\kappa$  of our simulations (red) against experiments (blue, Lutz *et al.* 2005) and theory (black, Bertelsen *et al.* 1973) in the finite DC layer thickness regime. Flow topology: Illustrations showing (d) a heteroclinic orbit and (e) a homoclinic orbit. Simulation details: domain  $[0, 1]^2$  m<sup>2</sup>, uniform grid spacing  $h = 1/2048$  m, penalization factor  $\lambda = 10^4$ , mollification length  $.pdfilon_{moll} = 2\sqrt{2}h$ , lagrangian CFL = 0.01, with viscosity  $\nu$  and oscillation frequency  $\omega$  set according to prescribed streaming Reynolds number ( $R_s$ ). The above values are used throughout the text, unless stated otherwise. We refer to Gazzola *et al.* (2011) for details on these parameters.

## B. Streaming flow topology: a dynamical systems view

We propose to characterize the streaming flow topologies generated by complex shape bodies via dynamical systems theory. First, we identify critical points in the flow field, i.e. points where the velocity is zero. These points offer a sparse yet complete representation of the flow field and its underlying dynamics [43]. Critical points can be classified into saddles and centres (depending on the local flow properties i.e. eigenvalues of the associated Jacobian), and the appearance and disappearance of their connecting streamlines shape the flow and its transitions. Figure 1(d, e) illustrates two cases of importance in our context: heteroclinic orbits defined as streamlines connecting two saddles, and homoclinic orbits defined as streamlines that connect a saddle to itself, thus forming an enclosed flow region. Parametric changes (shape symmetry, body curvature, back-

ground flow) lead to the displacement of critical points, which can cause the breaking, merging or collapsing of these orbits, and a consequent topological rearrangement.

As an illustrative example, we consider again the classical case of a single circular cylinder. Figure 1(*a, b*) depicts the critical points in the streaming flow field for Stokes-like and finite-thickness DC layer regimes, respectively. For reference, centres (vorticity-dominated) are denoted as diamonds and saddles (shear-dominated) as circles in figure 1(*a-e*). Compared to the Stokes-like regime, the finite-thickness DC layer regime presents four additional saddles (on the horizontal and vertical axes), that lie at a distance  $\delta_{DC}$  from the cylinder surface (figure 1(*c*)). Heteroclinic orbits between these saddles form a continuous circular streamline that cleanly separates the DC layer from the driven fluid, thus helping us to topologically distinguish the flows.

The above characterization allows us to investigate flow topology transitions using bifurcation theory. Since the two dimensional streaming flow in our setting is time-independent (streamlines  $\equiv$  pathlines) and incompressible (i.e a streamfunction exists), our system can be equivalently represented as an autonomous Hamiltonian system with  $H \equiv \Psi$ , where  $H$  and  $\Psi$  correspond to the Hamiltonian and time-averaged streamfunction, respectively [44]. Due to the  $H \equiv \Psi$  equivalence, orbits of streaming fluid particles (iso-contours of  $\Psi$ ) can be interpreted as iso-contours of  $H$ , enabling us to describe the local flow topology using the scalar function  $H(x, y)$  alone (which is conserved along a streamline or fluid orbit). We exploit this equivalence to map the transitions seen in our lattice system (§IV) to well-studied bifurcations in Hamiltonian systems. Once such a bifurcation is identified, we borrow the corresponding reduced Hamiltonian form  $H(x, y)$ , which mathematically captures topology changes near bifurcating critical points [45, 46]. This allows us to predict how the flow evolves upon perturbing shape curvature and/or background flow conditions. Moreover, the analysis of the reduced Hamiltonian form provides insight into the physical mechanisms at play, and guides our intuition of how to manipulate these systems.

#### IV. Lattice system: setup, phase space and flow bifurcations

##### A. Curvature variation setup: cylinders in an infinite, regular lattice

We systematically study body curvature effects via a system consisting of staggered circular cylinders of two radii,  $1/\kappa_{\max}$  and  $1/\kappa_{\min}$ , assembled into a periodic regular lattice (figure 2(*a*)), with  $\kappa_{\max}$  kept constant as a reference length scale. Throughout the study, the centre-to-centre distance  $s$  between these cylinders is kept constant as  $12.5/\kappa_{\max}$ , which allows us to vary the curvature ratio ( $\kappa_{\max}/\kappa_{\min}$ ) from 1 to 6. We note here that we performed cursory phase space explorations for different values of  $s$ , and observed that the qualitative nature of the emerging streaming fields is preserved, although the boundaries between different topological phases (see next sections) shift quantitatively. The oscillatory amplitude  $A$  for all the cylinders in the lattice is kept constant ( $A\kappa_{\max} = 0.1$ ).

A variation of  $\kappa_{\max}/\kappa_{\min}$  in the system manifests as a variation in the local AC layer thickness ( $\delta_{AC}\kappa_{\max} = A\kappa_{\max}/\sqrt{R_s}$  and  $\delta_{AC}\kappa_{\min} = A\kappa_{\min}/\sqrt{R_s}$ ), and thus in the DC layer thickness, with both affecting flow topology. With  $\kappa_{\max}/\kappa_{\min}$  capturing all geometric variation, and  $\delta_{AC}\kappa_{\max}$  capturing all background flow variation (§III A), we set to map the corresponding phase space. We hypothesize that the flow dynamics underlying this two discrete-curvatures setup will generalize to individual, complex shapes with a range of curvatures.

##### B. Lattice system: phase space

We proceed with the systematic variation of  $\delta_{AC}\kappa_{\max}$  and  $\kappa_{\max}/\kappa_{\min}$ , and span the phase space shown in figure 3(*h*). Here, we classify the observed flow topological patterns into distinct phases,



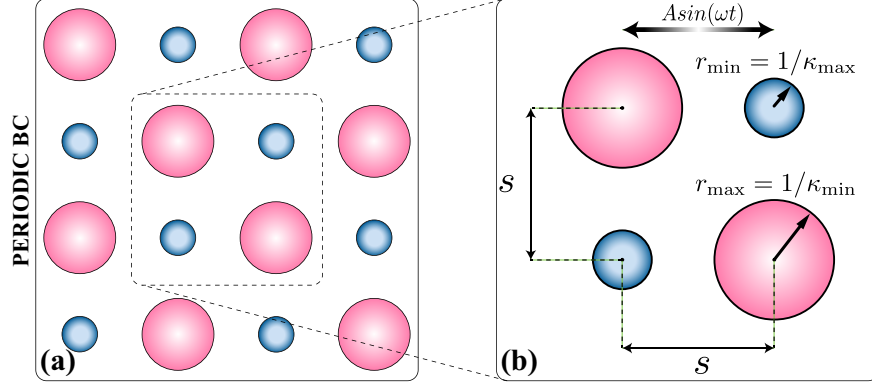


FIG. 2: Curvature variation setup. Illustrations of (a) computational domain and regular lattice with periodic boundary conditions. (b) A repeating unit cell of the lattice system with cylinders of two curvatures  $\kappa_{\max}$  and  $\kappa_{\min}$  and the fixed centre-to-centre spacing  $s = 12.5/\kappa_{\max}$ .

based on critical points and orbits. We observe seven main phases.

#### 1. Phase I

Figure 3(a) shows a representative flow pattern of Phase I. The flow around each cylinder is perfectly repeating due to constant curvature ( $\kappa_{\max}/\kappa_{\min} = 1$ ) and symmetry, and presents only the DC layers around the cylinder. This is a direct generalization of figure 1(a) to multiple, identical cylinders.

#### 2. Phase II

The flow is perfectly repeating around each cylinder on account of the constant curvature ( $\kappa_{\max}/\kappa_{\min} = 1$ ) and symmetry, and presents both the driven flow regions (separated by heteroclinic orbits) and the DC layers around the cylinder (figure 3(b)). This is a direct generalization of figure 1(b) to multiple, identical cylinders.

#### 3. Phase III

The DC layers of the smaller cylinders interact with each other, while those of the larger cylinders do not (figure 3(c)). This leads to the formation of a homoclinic orbit which joins the saddle at the centre of the unit cell to itself.

#### 4. Phase IV

The driven flow regions of the larger cylinders interact with each other (while those of the smaller cylinders do not), forming a homoclinic orbit which joins the saddle at the centre of the unit cell to itself (figure 3(d)). Additionally, around the smaller cylinders only the DC layers are observed.

#### 5. Phase V

The interaction of the driven flow regions of the larger cylinders forms a homoclinic orbit (figure 3(e)). Additionally, new driven flow regions are observed around the smaller cylinders. These buffer regions are separated from the smaller cylinders' DC layers and the homoclinic orbit regions via heteroclinic orbits.

#### 6. Phase VI

The driven flow regions of the larger cylinders merge to form a single vortical flow region (no homoclinic orbit), while only the DC layers are observed around the smaller cylinders (figure 3(f)).

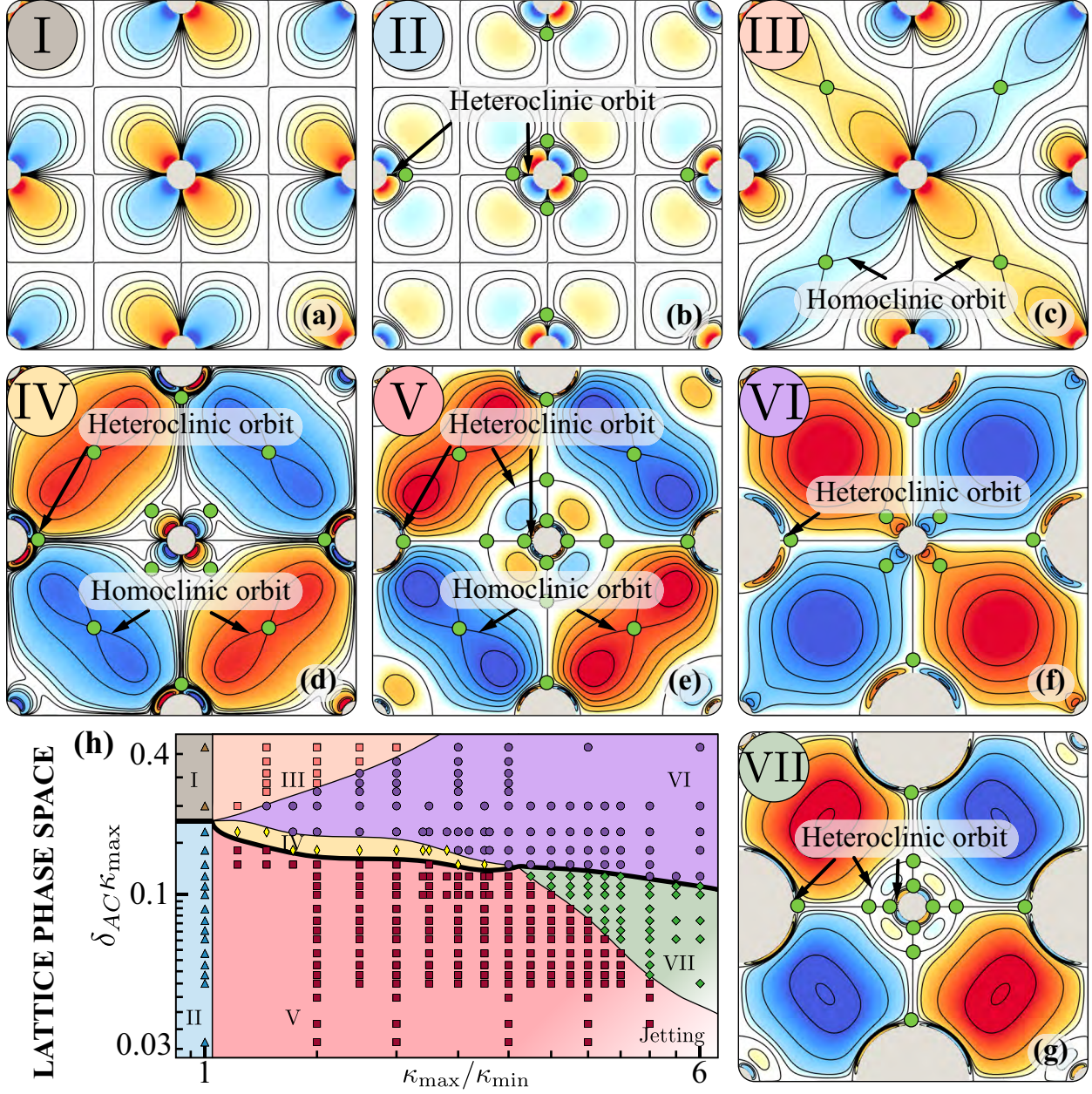


FIG. 3: Lattice phase space. The time-averaged streamline patterns depicted in (a-g) are classified into different phases depending on their flow topology. Defining connections and corresponding saddles (green circles) are highlighted in (a-g). (h) Phase space as a function of  $\delta_{AC}\kappa_{\max}$  and  $\kappa_{\max}/\kappa_{\min}$ . Black lines indicate transition boundaries between phases. The bold line indicates the existence of a hidden phase, which is characterized later.

#### 7. Phase VII

Along with the merging of the driven flow regions of larger cylinders (no homoclinic orbit), around the smaller cylinders both the buffer driven flow regions (separated by heteroclinic orbits) and the DC layers are observed (figure 3(g)).

#### 8. Hidden Phase

Besides the main seven phases reported above, we encounter a hidden phase along the  $I \rightarrow II$ ,  $IV \rightarrow V$  and  $VI \rightarrow VII$  boundaries. In our lattice setup, this phase is a very narrow sliver

characterized by fine flow structures. Since this phase would be hardly visible in our phase space, we indicate it as a marked bold line, and postpone its characterization when the corresponding flow transitions are analyzed in §IV C 4. Nonetheless, this phase is important and becomes more prominent when shapes other than circular cylinders are considered, as demonstrated in §V.

### 9. Jetting Regime

Finally, we note the presence of a jetting regime (bottom-right corner of the phase space), characterized by unsteady jets developing from the cylinder surface along the oscillation direction. This phenomenon is well-known [47, 48] and is captured by our solver [49]. However, the current study focuses on steady streaming phenomena and we will not be looking at jetting here.

In summary, we observe that curvature variations give rise to rich dynamics. This manifests in a variety of flow topologies that are not merely the superposition of streaming fields of the individual cylinders (Phase I and II), but also emerge from their non-linear interactions as a collective behavior response.

## C. Lattice system: flow bifurcations

Next, we characterize the topological transitions between phases from a dynamical systems perspective, using bifurcation theory.

### 1. Phase II $\rightarrow$ V: heteroclinic orbit bifurcation

We first consider the phase transition II  $\rightarrow$  V in figure 4(a). We draw attention to the presence of heteroclinic orbits in Phase II (figure 4(b)) and their absence in Phase V (figure 4(c)). The simplest Hamiltonian form that captures this transition, in terms of critical points, orbits and symmetry before and after, can be expressed as  $H(x, y) = xy^2 + ax + \beta y$  with  $a < 0$  [50]. Here  $\beta y$  is the unfolding term, which is added to the mathematical representation of the dynamical system to investigate its behaviour upon a perturbation [51]. As can be seen, if  $\beta = 0$  the Hamiltonian is perfectly symmetric about the horizontal and vertical axes ( $x = y = 0$ , located in the middle of figure 4(d)) and exhibits two saddles connected by a heteroclinic orbit. As the unfolding term deviates from zero ( $\beta \neq 0$ ) the orbit breaks up (figure 4(e)) and the system undergoes a heteroclinic orbit bifurcation [50], as observed in figure 4(c) and reflected in Phase V. The identification of the bifurcation type in mathematical terms provides insight into the mechanisms at play. Indeed,  $\beta \neq 0$  is physically interpreted as introducing asymmetry in the system, which we achieve through curvature variation ( $\kappa_{\max}/\kappa_{\min} > 1$ ). Nonetheless, symmetry can be broken in any number of ways, leading to the same flow topology rearrangement. As a demonstration (shown in the appendix), we recover the same orbit bifurcation by keeping  $\kappa_{\max}/\kappa_{\min} = 1$ , while breaking symmetry via a slow uniform background flow.

This example illustrates how the phase space combined with bifurcation analysis, can provide a set of rules to understand and manipulate streaming flow topology.

### 2. Phase V $\rightarrow$ VII: supercritical pitchfork bifurcation

We discuss the bifurcation Phase V  $\rightarrow$  VII, as depicted in figure 5(a). We draw attention to the presence of homoclinic orbits (with two enclosed centres and a saddle) in Phase V (figure 5(b)) and their absence (only one centre) in Phase VII (figure 5(d)). The simplest Hamiltonian form that captures this transition is  $H(x, y) = x^2 + \beta y^2 + y^4$ , which corresponds to a supercritical pitchfork bifurcation [52]. Here  $\beta y^2$  is the unfolding term, and represents the distance between the centres (figure 5(e-g)). In our lattice system, this distance can be directly controlled by increasing  $\kappa_{\max}/\kappa_{\min}$ , thus increasing the radii of the two opposite cylinders so as to push the centres towards the saddle in the middle of the cell (figure 5(c)), causing them to collide and destroy the homoclinic

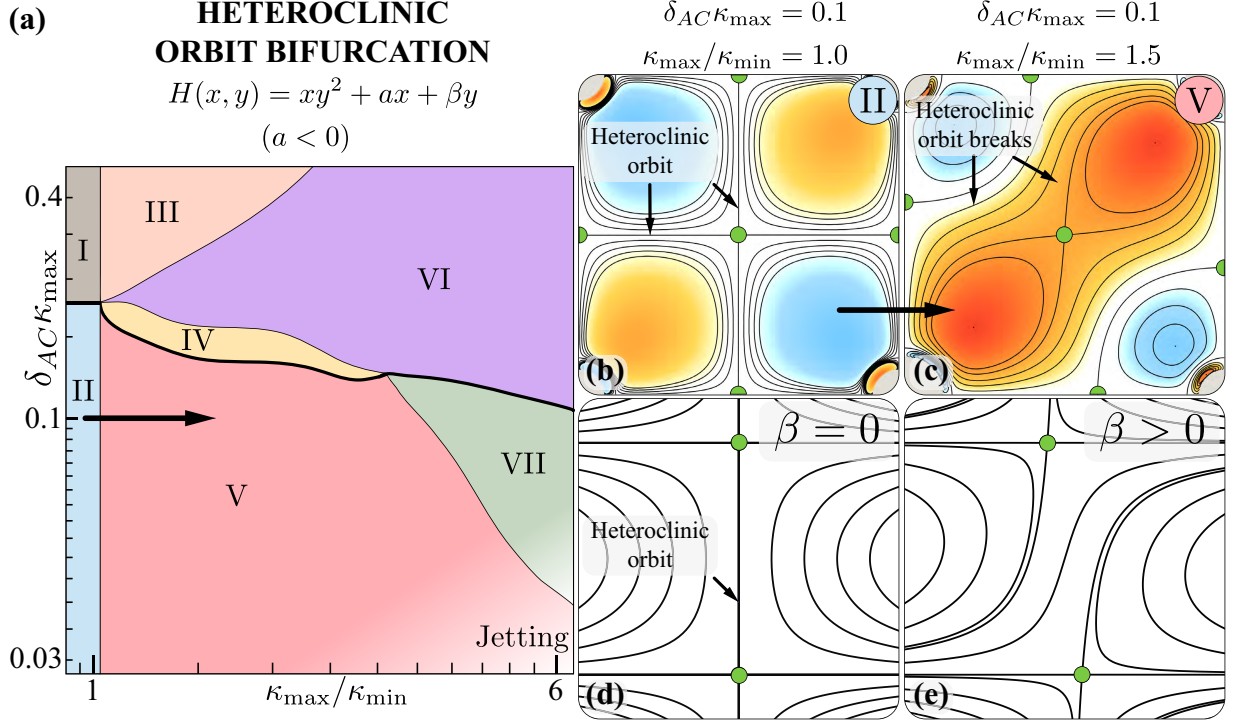


FIG. 4: Phase II  $\rightarrow$  V: heteroclinic orbit bifurcation. (a) The transition is highlighted on the phase space and the corresponding reduced Hamiltonian form is reported. (b, c) Flows representative of Phase II and V, respectively. (d, e) Bifurcations captured as contours of the reduced Hamiltonian form.

orbits (figure 5(d)). We observe that an equivalent flow topology rearrangement can be triggered by varying the background oscillatory flow. Indeed, by reducing the streaming Reynolds number  $R_s$  (i.e.  $\delta_{AC} \uparrow$ ), we can increase the thickness  $\delta_{DC}$  of the inner boundary layers around the cylinders, which in turn push the centres to collide with the saddle. As a consequence, the same supercritical pitchfork bifurcation is also encountered on increasing  $\delta_{AC}$  (dashed vertical arrow), explaining the fact that the boundary between Phase V and VII is inclined.

### 3. Phase III $\rightarrow$ VI: subcritical pitchfork bifurcation

We now investigate the bifurcation Phase III  $\rightarrow$  VI, as depicted in figure 6(a). We draw attention to the absence of a merged driven flow region in Phase III (figure 6(b)) and its presence (enclosed centre and two saddles) in Phase VI (figure 6(d)). The simplest Hamiltonian form that captures this transition is  $H(x, y) = x^2 + \beta y^2 - y^4$ , which corresponds to a subcritical pitchfork bifurcation [52]. Here  $\beta y^2$  is the unfolding term, which drives the appearance of the merged driven flow region ( $\beta > 0$ ) by modulating the distance between the saddles (figure 6(e-g)). In our lattice system, this appearance can be controlled by increasing  $\kappa_{\max}/\kappa_{\min}$ , which in turn decreases the thickness  $\delta_{DC}$  of the inner boundary layers around the larger cylinders. This pulls on the saddle in the middle (figure 6(b)), eventually splitting it into a center and two saddles (figure 6(c)), which are further pulled apart as the merged driven flow grows larger (figure 6(d)). An equivalent flow topology rearrangement can be achieved by modulating the background flow so as to directly decrease  $\delta_{AC}$  and the thickness  $\delta_{DC}$  of the inner boundary layers, again pushing the saddles apart and causing the appearance of a merged driven flow. As a consequence, the same subcritical pitchfork bifurcation is encountered on decreasing  $\delta_{AC}$  (dashed vertical arrow), explaining the fact that the boundary between Phase III and VI is inclined.



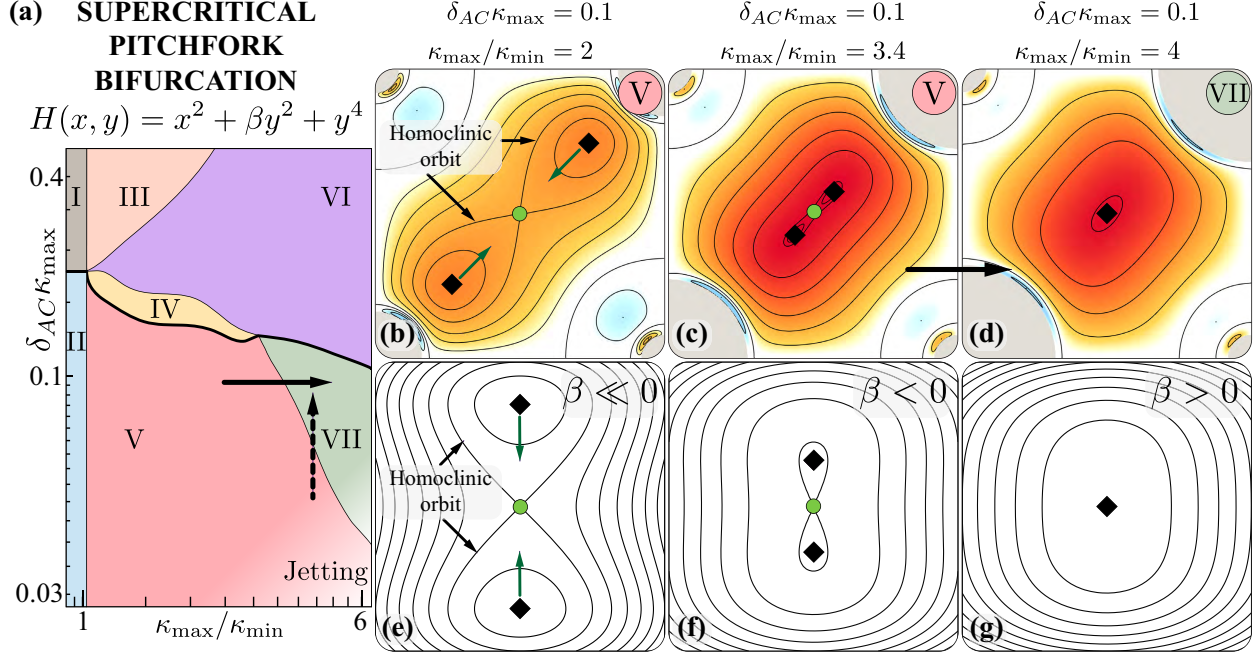


FIG. 5: Phase V  $\rightarrow$  VII: supercritical pitchfork bifurcation. (a) The transition is highlighted on the phase space and the corresponding reduced Hamiltonian form is reported. (b, c, d) Flows representative of Phase V, Phase V approaching the transition, and Phase VII, respectively. (e, f, g) Bifurcations captured as contours of the reduced Hamiltonian form. This bifurcation can also be triggered by varying the background oscillatory flow (i.e. by increasing  $\delta_{AC}$ , illustrated with a dashed vertical arrow in (a)), which is reflected in the phase space as an inclined transition boundary.

#### 4. Phase VI $\rightarrow$ VII: reflecting umbilic bifurcation

Here, we illustrate the bifurcation Phase VI  $\rightarrow$  VII, as depicted in figure 7(a). To identify this bifurcation we focus only on the region local to the smaller cylinder. We note the absence of a buffer driven flow region around the smaller cylinder in Phase VI (figure 7(b)) and its presence in phase VII (figure 7(k), marked in red). This flow topology change occurs in two consecutive s.pdf, passing through the hidden phase of §IV B 8.

In the first step, we draw attention to the absence of recirculating region pairs in Phase VI (figure 7(b)) and their presence in figure 7(d) (marked in red and comprising two saddles and two centers). We note that the latter flow field corresponds to the hidden Phase H. The simplest Hamiltonian form that captures this transition is  $H(x, y) = axy^2 + bx^3 + \beta x$  with  $ab > 0$ , which corresponds to a hyperbolic reflecting umbilic bifurcation [45]. Here  $\beta x$  is the unfolding term, that controls the appearance (going from  $\beta > 0$  to  $\beta < 0$ ) of the recirculating region pairs and their size (figure 7(e-g)). In our lattice system, the appearance and size of these regions can be controlled by decreasing  $\delta_{AC}$ , which decreases the DC layer thickness  $\delta_{DC}$  of both small and large cylinders. This pulls the streamlines adjacent to the small cylinders's DC layers in two opposite directions (figure 7(c)), forming a degenerate saddle on the vertical axis, which eventually splits into two saddles and two centres (figure 7(d)). Topologically, this manifests as a pair of counter-rotating recirculating regions. An equivalent flow topology rearrangement can be alternatively achieved by decreasing  $\kappa_{\max}/\kappa_{\min}$ , which increases the distance between the cylinder surfaces. This again pulls the streamlines in the above described fashion, triggering the same bifurcation. As a consequence, the same hyperbolic reflecting umbilic bifurcation is also encountered on decreasing  $\kappa_{\max}/\kappa_{\min}$  (dashed horizontal arrow), explaining the fact that the transition boundary is inclined.

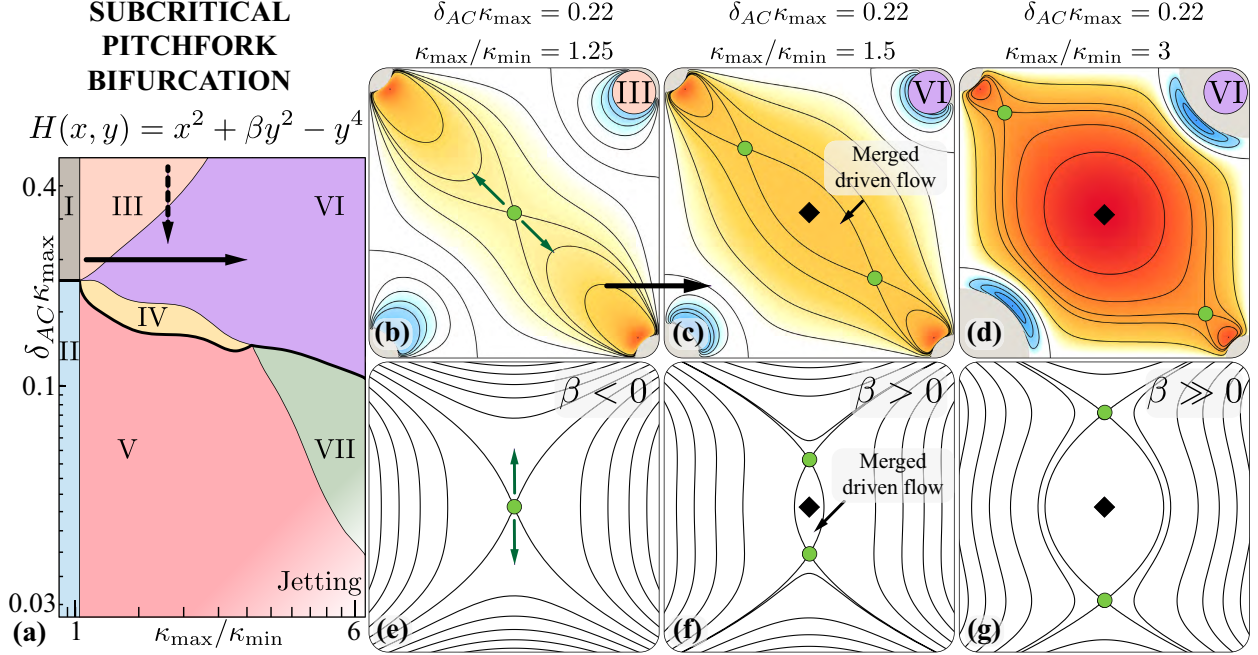


FIG. 6: Phase III  $\rightarrow$  VI: subcritical pitchfork bifurcation. (a) The transition is highlighted on the phase space and the corresponding reduced Hamiltonian form is reported. (b, c, d) Flows representative of Phase III, Phase VI approaching the transition, and Phase VI, respectively. (e, f, g) Bifurcations captured as contours of the reduced Hamiltonian form. This bifurcation can also be triggered by varying the background oscillatory flow (i.e. by increasing  $\delta_{AC}$ , illustrated with a dashed vertical arrow in (a)), which is reflected in the phase space as an inclined transition boundary.

The second step of the Phase VI  $\rightarrow$  VII transition occurs right after further decreasing  $\delta_{AC}$ , rendering the hidden Phase H very narrow. We focus on the highlighted saddles close to the horizontal axis in the hidden Phase H (figure 7(i)). After the transition these saddles are located on the horizontal axis, thus recovering Phase VII (figure 7(k)). The simplest Hamiltonian form that captures this rearrangement is  $H(x, y) = axy^2 + bx^3 + \beta x$  with  $ab < 0$ , which corresponds to an elliptic reflecting umbilic bifurcation [45]. Here  $\beta x$  is the unfolding term, that captures whether the saddles are present ( $\beta < 0$ ) or absent ( $\beta > 0$ ) on the horizontal axis (figure 7(l-n)), as well as their distance. Similar to the previous step, a decrease in  $\delta_{AC}$  causes a pull on the streamlines immediately adjacent to the small cylinder's DC layers. This time though, we do not observe a formation of degenerate saddles on the horizontal axis. This is due to the asymmetry resulting from the recirculating region pairs (marked in red in figure 7(i-k)) generated at the previous step. Instead, the saddles are now pushed towards the horizontal midplane, extending the recirculating region pairs. Upon reaching the midplane, the two opposite saddles collapse (figure 7(j)) and split along the horizontal axis (figure 7(k)). These new saddles together with the one formed at the previous step, completely define the buffer driven flow region around the smaller cylinder. Again, an equivalent flow topology rearrangement can be achieved by decreasing  $\kappa_{\max}/\kappa_{\min}$ . As a consequence, the same elliptic reflecting umbilic bifurcation is also encountered on decreasing  $\kappa_{\max}/\kappa_{\min}$  (dashed horizontal arrow), explaining the fact that the transition boundary is inclined.

We note here that the order (upon decreasing  $\delta_{AC}$ ) of these transitions is robust: first the hyperbolic and then the elliptic reflecting umbilic bifurcation. Nonetheless, the location at which they take place may vary. In our example the recirculating pairs are formed at the top/bottom of the cylinder, and then extend towards the horizontal midplane. Alternatively the pairs may form on the left/right of the cylinder and then grow towards the vertical midplane. More details can be

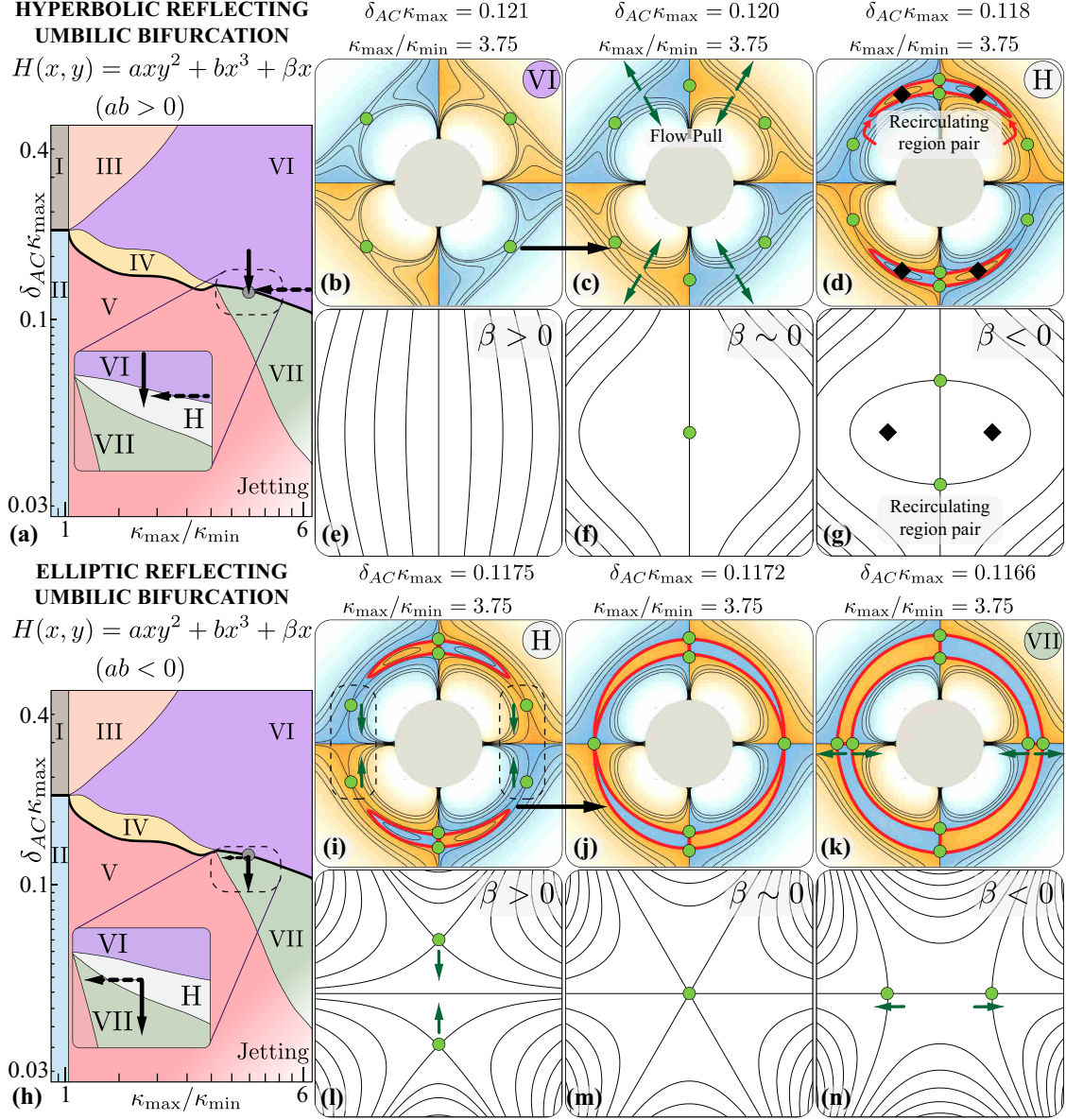


FIG. 7: Phase VI  $\rightarrow$  hidden Phase H: hyperbolic reflecting umbilic bifurcation. (a) The transition is highlighted on the phase space (with a zoomed in view) and the corresponding reduced Hamiltonian form is reported. (b, c, d) Flows (coloured in a logarithmic scale) representative of Phase VI, at the transition, and hidden Phase H, respectively. (e, f, g) Bifurcations captured as contours of the reduced Hamiltonian form. (h) The transition from hidden Phase H  $\rightarrow$  VII (elliptic reflecting umbilic bifurcation) is highlighted on the phase space (with a zoomed in view) and the corresponding reduced Hamiltonian form is reported. (i, j, k) Flows representative of hidden Phase H, at the transition, and Phase VII, respectively. (l, m, n) Bifurcations captured as contours of the reduced Hamiltonian form. These bifurcations can also be triggered by varying the curvature (i.e by varying  $\kappa_{\max}/\kappa_{\min}$ , a horizontal dashed arrow in (a, h)), which is reflected in the phase space as an inclined transition boundary. The newly created recirculating region pairs are marked in red.

found in the appendix.

### D. Summary of bifurcations

In the previous sections we identified all the bifurcations at play in our system, by focusing on a few particular phase transitions. In figure 8 we classify all phase transitions, completing our analysis. Therefore, figure 8 provides a compact rulebook to manipulate streaming flows based on curvature ( $\kappa_{\max}/\kappa_{\min}$ ) and background oscillatory flow ( $\delta_{AC}\kappa_{\max}$ ) variations.

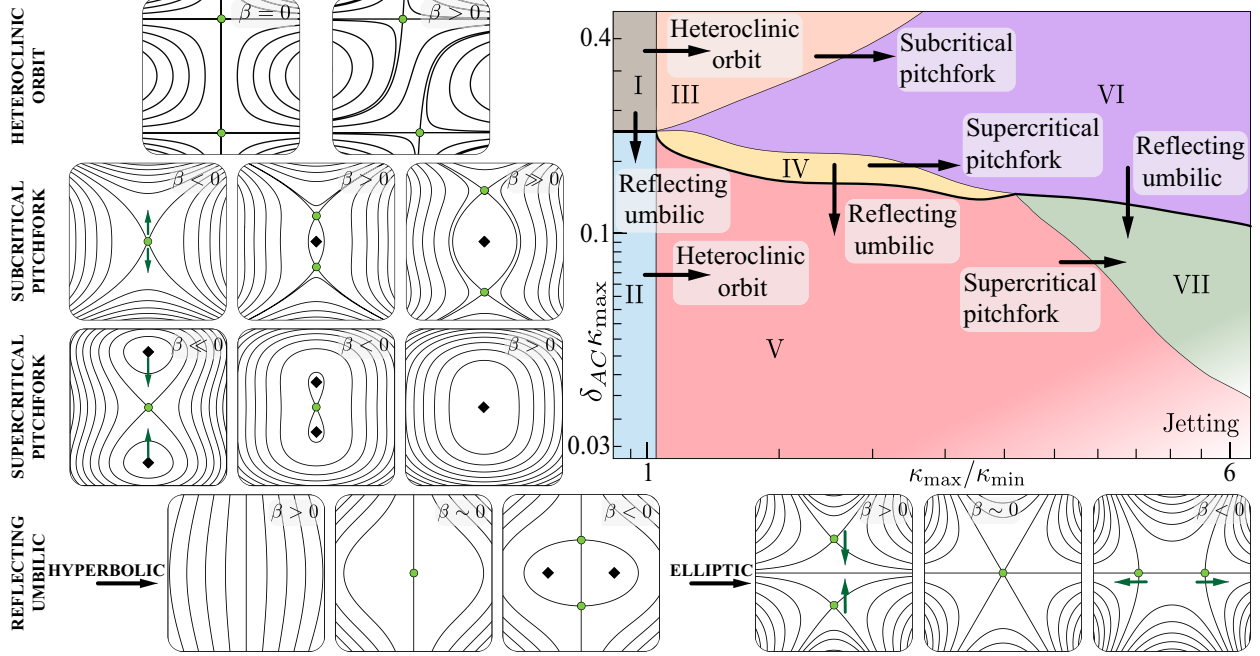


FIG. 8: Summary of the bifurcations seen in the lattice phase space.

### V. Generalization to individual convex streaming bodies

We now hypothesize that the above insights generalize to convex complex shapes immersed in an unbounded flow. When considering a given shape, we proceed as follows: we identify a local structure of interest, map it onto our phase space, predict how it will evolve based on local body curvature change or background flow variation, and verify the outcome by comparing with experiments and simulations.

#### A. Comparison against experiments: streaming triangles and squares

We first consider an individual equilateral triangle (of side length  $2a$ ), an object characterized by top-down asymmetry and extreme ratio of curvatures, from sharp vertices ( $\kappa_{\max} \rightarrow \infty$ ) to flat sides ( $\kappa_{\min} \rightarrow 0$ ). In the original experiments performed by Tatsuno (1975), this geometry was subject to oscillations and three different flow topologies were observed for increasing  $\delta_{AC}/a$ , from 0.05 to 1.06 (figure 9(d-f)). In figure 9(d) we focus on the highlighted saddle and the two centres near the horizontal edge of the triangle. This structure closely resembles the hidden Phase H of figure 7(d, g), where the second saddle (not imaged in experiments) approaches from infinity (figure 9(a)). We then map this structure onto our phase space (figure 9(j)) and employ our previous analysis to predict the behavior of these critical points as  $\delta_{AC}/a$  is increased, similar to the experiments. Based on our phase space (figure 8), as  $\delta_{AC}/a$  increases the distance between critical points reduces, bringing the saddle within the imaged domain (figure 9(b)) and forming a closed recirculating region, near the horizontal edge. Upon a further increase of  $\delta_{AC}/a$ , we predict that



the system will transition to a new topology corresponding to Phase VI, via a hyperbolic reflecting umbilic bifurcation (figure 9(c)). This is a consequence of the saddles and centres moving closer and closer, eventually collapsing and vanishing. Both experiments and simulations indicate that the system indeed behaves according to this picture, confirming our predictions (figure 9(d-i)).

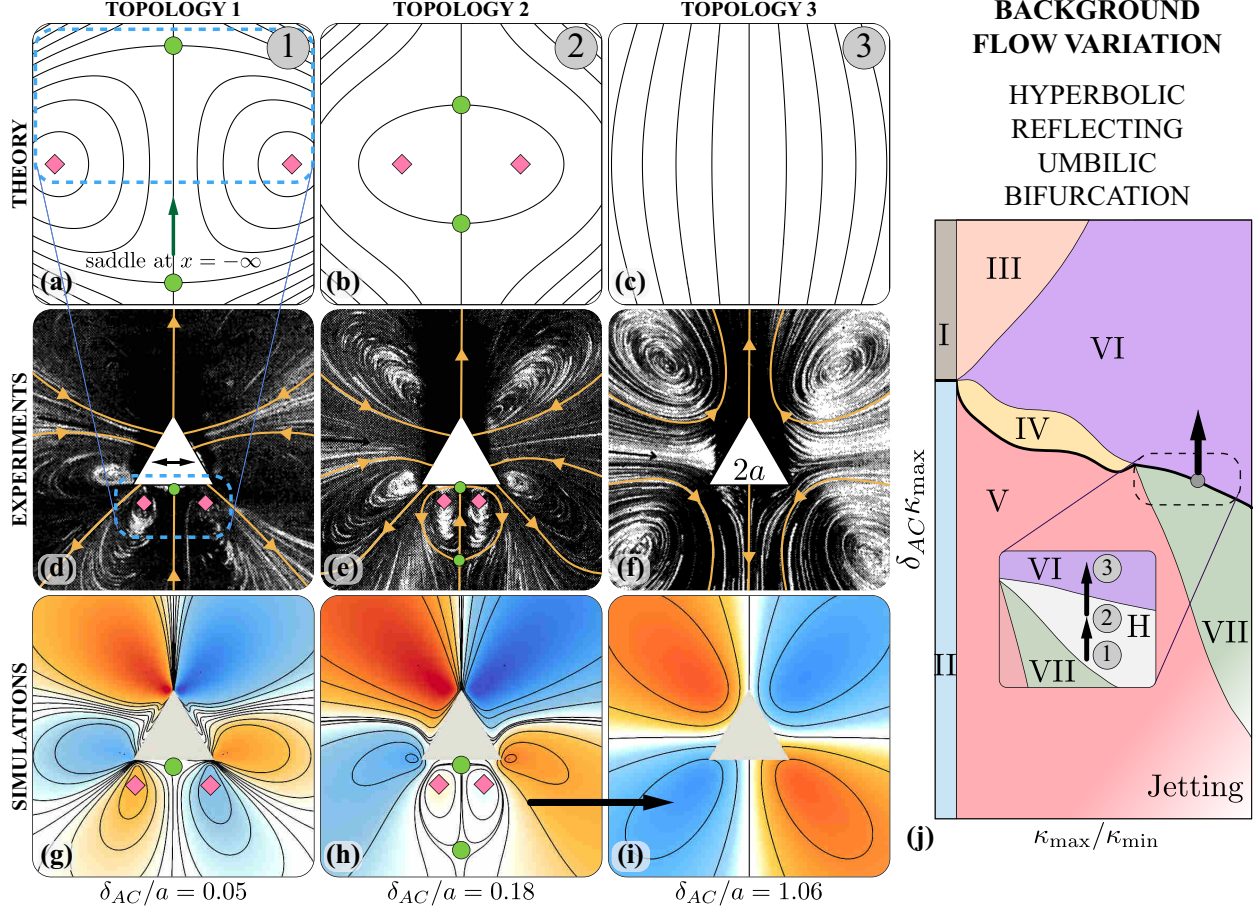


FIG. 9: Background flow variation for a triangle shaped cylinder. (a, b, c) present the reduced Hamiltonian form contours for hyperbolic reflecting umbilic bifurcation, associated with the transition hidden Phase H  $\rightarrow$  Phase VI in the lattice phase space. A topologically equivalent transition is observed on varying  $\delta_{AC}/a$ , both in experiments (d, e, f), and simulations (g, h, i). (j) Mapping of the observed transition on the lattice phase space.

We further test our understanding, this time against experiments involving an oscillating square cylinder (of side  $2a$ ) [12]. Similar to the case of the triangle, three different flow topologies are observed for increasing  $\delta_{AC}/a$ . Figures 10(c, d) and 11(c, d) report the corresponding experimental recordings. We first consider the case of figure 10(c, d) in which  $\delta_{AC}/a$  was varied from 0.18 to 1.42. This case closely resembles the dynamics associated with the triangle: indeed the highlighted saddles and centres (this time near both the top and bottom horizontal edges) can be mapped to the hidden Phase H of figure 7(d, g) and, as  $\delta_{AC}/a$  increases, undergo the same hyperbolic reflecting umbilic bifurcation, annihilating each other. Again, predictions, experiments and simulations agree (figure 10(c-f)). We note that the fact that identical local geometrical features affect the flow in a consistent fashion across globally different shapes (triangles and squares) points at the robustness of our approach. Finally, we consider the case of figure 11(c, d) of a square cylinder at  $\delta_{AC}/a = 0.05$  and 0.18. We focus on the highlighted saddles forming a recirculation zone near the vertical sides of the square. This structure closely resembles Phase VII of figure 7(k, n), where the second

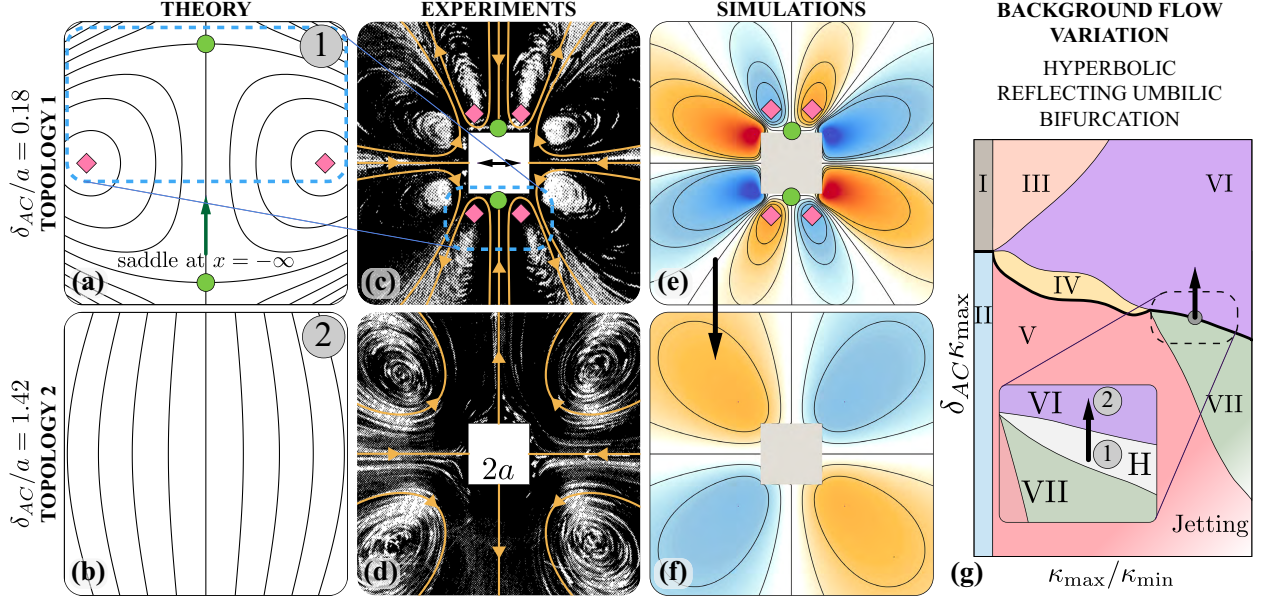


FIG. 10: Background flow variation for a square shaped cylinder. (a, b) present the reduced Hamiltonian form contours for hyperbolic reflecting umbilic bifurcation, associated with the transition hidden Phase H  $\rightarrow$  Phase VI in the lattice phase space. A topologically equivalent transition is observed on varying  $\delta_{AC}/a$ , both in experiments (c, d) and simulations (e, f). (g) Mapping of the observed transition on the lattice phase space.

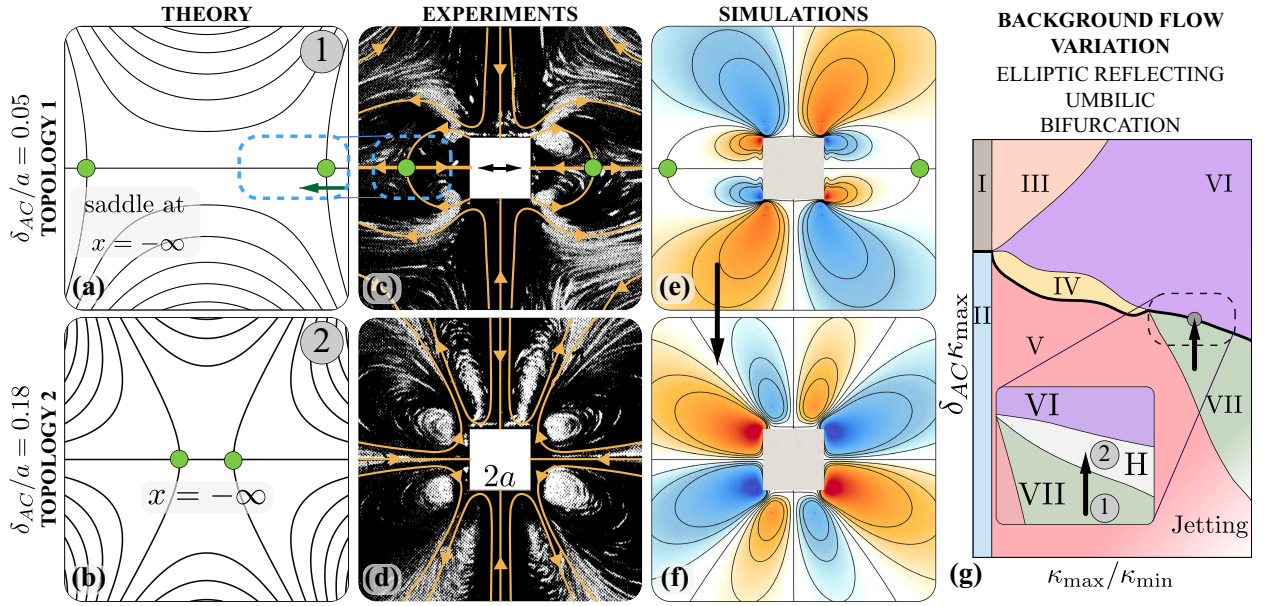


FIG. 11: Background flow variation for a square shaped cylinder. (a, b) present the reduced Hamiltonian form contours for elliptic reflecting umbilic bifurcation, associated with the transition VII  $\rightarrow$  hidden Phase H in the lattice phase space. A topologically equivalent transition is observed on varying  $\delta_{AC}/a$ , both in experiments (c, d) and simulations (e, f). (g) Mapping of the observed transition on the lattice phase space.

saddle (not imaged in experiments) is located at infinity. Thus, as  $\delta_{AC}/a$  increases, we predict that the saddles near the square will progressively move outwards, to approach the saddles at infinity and undergo an elliptic reflecting umbilic bifurcation (figure 11(b)). This has the overall effect to

enlarge the recirculation zone on the sides of the square. Once again, experiments and simulations confirm our intuition (figure 11(c-f)).

We note here that in all these cases Phase H is not as narrow as in our lattice system. This is not inconsistent: indeed we expect the phase boundaries to shift quantitatively for globally different geometries, and our analysis holds as long as the phase space structure is locally preserved. Although we cannot mathematically prove that the phase space organization is retained in any generic setting, we complemented the investigations presented here with a number of other studies (presented in the appendix for brevity), and all of them were found to be consistent with our analysis. This empirical validation underscores the practical use of our approach for flow design and manipulation purposes, as further exemplified in the next section.

### B. Rational design of a streaming-enhanced transport bot

In a recent study, we illustrated how a ‘bullet’ shaped streaming bot enhances fluid mediated transport of passive particles relative to simple circular cylinders [34]. The bullet geometry was empirically determined based on experiments on triangles [13], from which we borrowed fore-aft asymmetry and high rear curvature profiles. The rationale was to reproduce the closed streaming recirculation region observed in figure 9(e,h) to effectively trap trailing particles and favor their transport as the bot displaces forward. Here, we elucidate how that flow topology and object geometry could have been rationally designed based on our phase space, in a step by step fashion.

Figure 12(a) illustrates our design process of morphing a circular cylinder into a circular-square hybrid cylinder (bullet). This hybrid cylinder presents top-down asymmetry—the top side is a circle with constant curvature  $\kappa_0$ , while the bottom is a square with rounded corners of constant curvature  $\kappa_v$ . Hence specifying  $\kappa_v/\kappa_0$  characterizes the shape geometry—for  $\kappa_v/\kappa_0 = 1$  the body is a perfect circle, while for  $\kappa_v/\kappa_0 > 1$  the body presents a range of curvatures  $\in [0, \kappa_v]$  on its bottom half. To completely characterize this system, we capture the background flow variation using  $\delta_{AC}\kappa_v$ , similar to the lattice phase space.

In the following, we break down the morphing design process in s.pdf. Each one of them relates a geometric or background flow variation to a corresponding local flow topology change, for which we highlight the concerned critical points and orbits.

#### 1. Step ① $\rightarrow$ ②

We start by choosing a  $\delta_{AC}\kappa_{\max}$  for which the streaming flow topology for a circular cylinder ( $\kappa_v/\kappa_0 = 1$ ) lies in the finite-thickness DC layer regime. This corresponds to Phase II in figure 12(a). With in mind the goal of reshaping the overall flow topology to mimic the favourable features of figure 9(e, h), the first step is to “open up” the DC layer. We then focus on the highlighted heteroclinic orbits in figure 12(b). Recalling our observations in the lattice phase space, we predict that breaking top-down symmetry ( $\kappa_v/\kappa_0 > 1$ ) will break these orbits via a heteroclinic orbit bifurcation (Phase II  $\rightarrow$  V of figure 8). This is computationally confirmed in figure 12(c), and has the effect of unfolding horizontally the two bottom recirculating regions of the DC layer.

#### 2. Step ② $\rightarrow$ ③

Next, we need to prepare the conditions to form the closed flow region behind the cylinder (similar to figure 9(d, g)). This can be achieved by collapsing the newly generated saddles and centers. Their annihilation will cause the unfolded DC layer pockets to merge with the top driven flow regions. This, in turn, pushes the bottom driven flow regions against each other, compressing and aligning them vertically (and eventually connecting them at infinity via a saddle point). We then focus on the highlighted saddles and centres of figure 12(c), which closely resemble Phase V of figure 5(b). We predict that a further increase in  $\kappa_v/\kappa_0$  will result in the saddle and centre approaching each other and eventually colliding, leading to a saddle-centre bifurcation (Phase



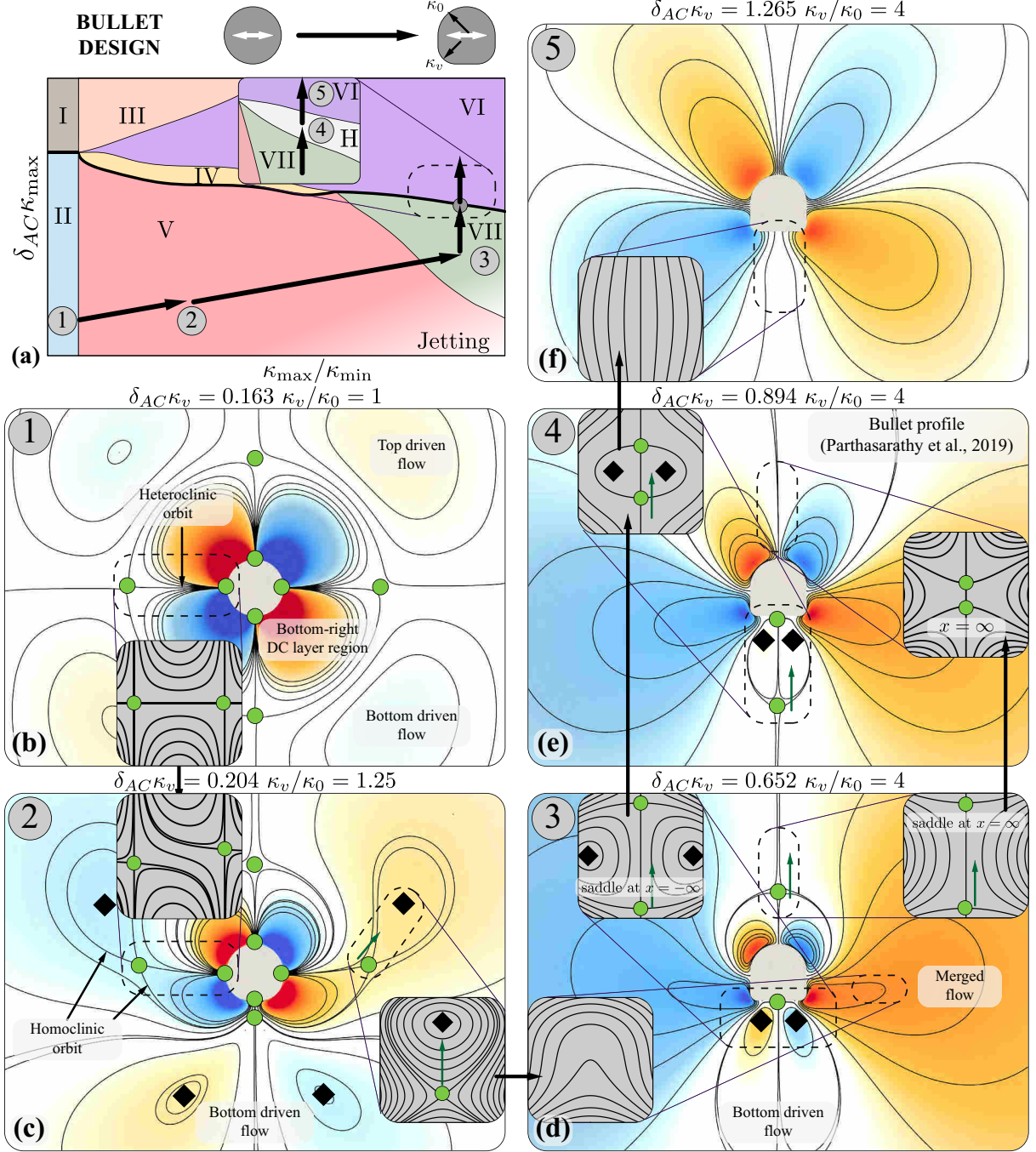


FIG. 12: Flow topology manipulation. (a) Illustration of morphing a circular cylinder into a circular-square hybrid shaped cylinder with a circular side and a square side. Mapping of the observed transitions on the lattice phase space. (b-f) Different topologies observed on geometric and background flow variation, with the concerned critical points highlighted and the predictions (reduced Hamiltonian form contours) illustrated as grey contours.

$V \rightarrow VII$  of figure 8). The occurrence of this bifurcation, with the subsequent flow topology rearrangement, is indeed numerically confirmed in figure 12(d).

### 3. Step ③ $\rightarrow$ ④

Now the flow is favorably rearranged. In order to recover the useful closed flow region of figure 9(e, h), we need to bring closer to the streaming body the saddle that connects at infinity the bottom driven flow regions. We then focus on the highlighted saddles and two centres near the horizontal edge of the bullet in figure 12(d), which closely resembles the hidden Phase H of figure 7(d) (with one saddle at infinity) or figure 9(a, d). Then a background flow variation ( $\delta_{AC} \uparrow$ ) pulls the saddle upwards, closer to the body, as predicted (figure 12(e)). Additionally, we note that the flow structure in front (top) of the streaming shape can be mapped to Phase VII of figure 7(k). Therefore, as a side effect of the increase in  $\delta_{AC}$ , the saddle in front of the body is pushed away upwards, eventually (next step) undergoing the elliptic reflecting bifurcation (Phase VII  $\rightarrow$  hidden Phase H) observed in figure 7(j) and figure 11(d, f). Computations of figure 12(e) confirm this intuition.

### 4. Step ④ $\rightarrow$ ⑤

Finally, in addition to controlling the size of the closed flow region as discussed above, we now demonstrate (for completeness) how we can further manipulate its presence or absence. We focus on the highlighted saddles and the two centres near the horizontal edge of the bullet (figure 12(e)), which closely resemble the hidden Phase H of figure 7(d). Then a background flow variation ( $\delta_{AC} \uparrow$ ) results in the saddles and centres approaching each other to then collapse, thus making the closed flow region disappear. This is computationally confirmed in figure 12(f), which validates our prediction of a hyperbolic reflecting umbilic bifurcation (hidden phase H  $\rightarrow$  Phase VI, figure 7(b), figure 9(f, i) and figure 10(d, f)).

In summary, this section illustrates how our approach can be employed to predict and design streaming flow topologies, in a rational fashion.

## VI. Conclusions

With the goal of extending our understanding of streaming phenomena to include body curvature effects, we propose a simplified setting in which multiple circular cylinders are regularly arranged in a periodic lattice. We systematically investigate this system to construct a phase space that relates local body curvature and background flow variations to streaming flow topology. The obtained phase space reveals rich dynamics on account of the non-linear, collective behavior that stems from the presence of multiple body length scales. The phase space is subsequently analyzed through the lens of dynamical system theory, to detect the bifurcations and physical mechanisms at play. We then demonstrate that our understanding in the simplified lattice system can be extended to individual bodies presenting a spectrum of curvatures. Altogether these results provide physical intuition and a rulebook to manipulate and design streaming flow topologies, which may find useful application in microfluidics and micro-robotics.

Although our study provides a systematic prediction of flow topology transitions on geometric and background flow variation, our understanding still remains incomplete. How do we incorporate concave geometric features? How does our approach extend to three-dimensional settings? How does body topology affect flow topology? These questions are beyond the scope of the current paper, and are avenues of future research.

## VII. Acknowledgements

We thank Sascha Hilgenfeldt for helpful discussions over the course of this work. The authors acknowledge support by the National Science Foundation under NSF CAREER Grant No. CBET-1846752 (MG) and by the Blue Waters project (OCI- 0725070, ACI-1238993), a joint effort of the University of Illinois at Urbana-Champaign and its National Center for Supercomputing Applica-

tions. This work used the Extreme Science and Engineering Discovery Environment (XSEDE) [53] Stampede2, supported by National Science Foundation grant number ACI-1548562, at the Texas Advanced Computing Center (TACC) through allocation TG-MCB190004.

## VIII. Appendix

### A. Curvature variation setup: cylinders in an infinite regular lattice

Here we provide further details relative to our setup, which consists of a lattice of cylinders with two discrete curvatures. With a computational domain of range  $[0, 1]$ , we instantiate a lattice of 16 cylinders in a  $4 \times 4$  grid with periodic boundary conditions. To accommodate 4 cylinders in our domain, while allowing a curvature variation up to  $\kappa_{\max}/\kappa_{\min} = 6$ , we fix  $\kappa_{\max} = 0.02$  as a reference length scale. Then the constant centre-to-centre distance between these cylinders is  $s = 1/4 = 0.25 = 12.5\kappa_{\max}$ . Maintaining  $s$  constant allows us to consistently compare systems characterized by different curvature ratios. The value of  $s$  is chosen to span a reasonable curvature ratio range, and at the same time is practical from an experimental, fabrication standpoint. The oscillatory amplitude ( $A$ ) for all the cylinders in the lattice is kept constant ( $A\kappa_{\max} = 0.1$ ). This is because oscillating the fluid with constant amplitude is experimentally convenient. By virtue of keeping a constant amplitude, the streaming flow for the lattice system can be characterized with one value of  $R_s$  ( $R_s = A^2\omega/\nu$ ). Lastly, fixing a constant amplitude allows us to extend our understanding (with two curvatures) to individual complex shapes with multiple curvatures. Indeed all local curvatures of an individual streaming body undergo the same absolute oscillation amplitudes. We note here that we performed cursory phase space explorations for different spacings between cylinders, and observed that the qualitative nature of the emerging streaming fields is preserved, although the boundaries between different topological phases shift quantitatively.

### B. Lattice system: flow bifurcations

#### 1. Heteroclinic orbit bifurcation via asymmetric background flow

Here we revisit the heteroclinic orbit bifurcation observed for the transition  $\text{II} \rightarrow \text{V}$  of figure 4 in the main text. We identified the reduced Hamiltonian form with the unfolding term coefficient  $\beta$  that represents symmetry ( $\beta = 0$ ) or asymmetry ( $\beta \neq 0$ ) in our lattice setup (figure 13(a, b)). We now demonstrate that the notion of breaking symmetry extends to more than just curvature variation, by breaking symmetry via the superposition of a uniform background flow. Figure 13(c) presents a Phase II flow topology. We focus on the highlighted saddles and the heteroclinic orbits joining them. As we break symmetry along the horizontal axis by imposing a slow mean flow, we observe the predicted flow topology change (figure 13(d)), where the vertically oriented heteroclinic orbits break up, while the horizontally oriented ones do not. Through this illustration, we demonstrate that the control on asymmetry via means other than curvature variation leads to identical flow topology rearrangements. This confirms the physical intuition provided by the identified reduced Hamiltonian form.

#### 2. Reflecting umbilic bifurcation: two step rationale

We now focus on the transition between Phase VI and VII in the lattice phase space. We notice that the system appears symmetric about the horizontal and vertical axes. Yet, the transition into Phase VII occurs in two distinct steps: 1) a hyperbolic reflecting umbilic bifurcation that involves a topological rearrangement about the vertical axis of symmetry of the cylinder, and 2) an elliptic reflecting umbilic bifurcation that involves a topological rearrangement about the horizontal axis of symmetry of the cylinder. To investigate this preference for one axis over another, we focus on figure 14(a), which depicts the flow topology near the smaller cylinder in Phase VI. We focus on the highlighted saddles and the corresponding local flow topology depicted in figure 14(b). We

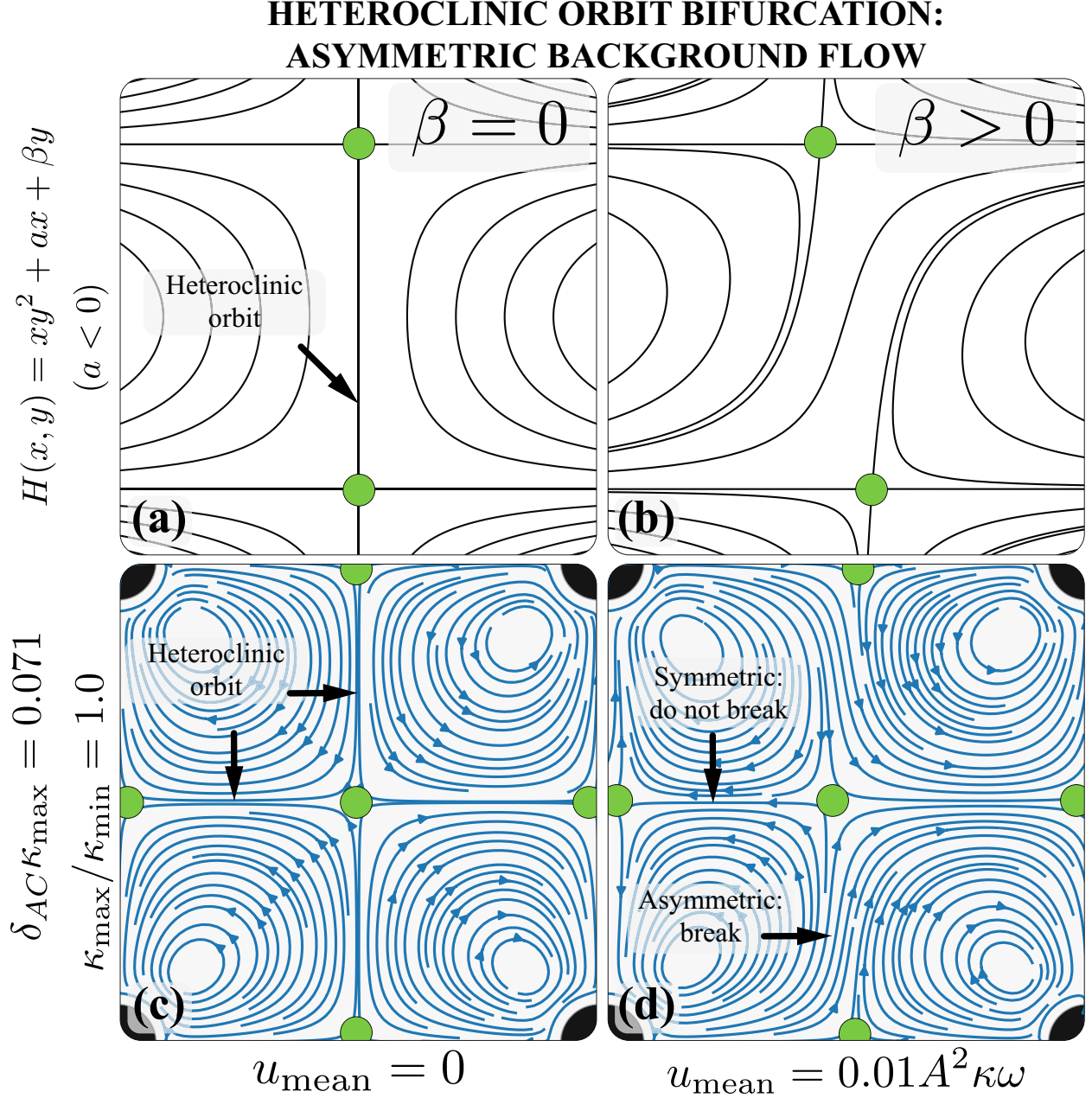


FIG. 13: Asymmetric background flow. We demonstrate that the heteroclinic orbit bifurcation, associated with the transition  $\text{II} \rightarrow \text{V}$  in the lattice phase space, can be triggered by breaking symmetry via superimposing a slow uniform background flow, instead of using curvature variations as in the main text. (a, b) present the reduced Hamiltonian form for the bifurcation, with the flow topology change on imposing the mean flow in the lattice system, shown in (c, d). We note that in (c, d) all cylinders present the same radius so that  $\kappa_{\max}/\kappa_{\min} = 1$ .

notice a small yet non-negligible difference between the angular location of the highlighted saddle in simulations ( $\theta_s$ ), and the expected location ( $\theta_i$ ) based on the symmetry of the setup. Upon increasing simulation's resolution, or varying background flow oscillation direction, the magnitude of this angular deviation can be reduced, but not removed, so that a small preference persists. We attribute this small preferential deviation to the fact that the cylinders location is not (and cannot be) perfectly aligned with the discretization grid.

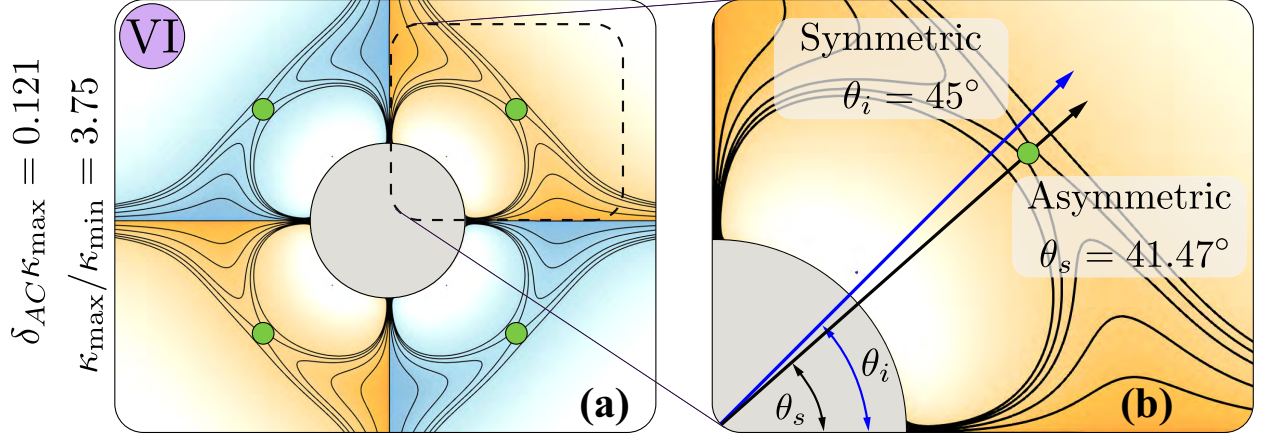


FIG. 14: Reflecting umbilic bifurcation. (a) Illustration of the flow topology near the smaller cylinder for Phase VI. (b) Angular location of the highlighted saddle observed in simulations  $\theta_s$ , compared to the expected symmetric location  $\theta_i$ . This small yet non-negligible difference creates asymmetry between the flow topology along the vertical and horizontal axes, resulting in the two step reflecting umbilic bifurcation.

This small local deviation from symmetry is responsible for the observed sequence of umbilic bifurcations. The sequence order is found to be robust: indeed a saddle misalignment with respect to the  $45^\circ$  angle consistently triggers the hyperbolic reflecting umbilic bifurcation first (as  $\delta_{AC}\kappa$  decreases), either on the vertical or horizontal axis, depending on  $\theta_s < 45^\circ$  or  $\theta_s > 45^\circ$ . The induced local topological rearrangement is then found to be the natural precursor of the elliptic reflecting umbilic bifurcation, which occurs on the axis perpendicular to the first bifurcation. Therefore, to summarize, the boundaries between Phase VI, hidden Phase H and Phase VII are robustly associated with the bifurcation identified in the main text, as empirically verified though the comparison with triangle and square experiments. We note that in a perfect lattice, this series of two s.pdf may coalesce in a single step. Nonetheless, this is only a theoretical scenario which we could not attain computationally and that cannot be expected to manifest experimentally.

### 3. Phase I $\rightarrow$ II: higher order reflecting umbilic bifurcation

Here, we illustrate the bifurcation Phase I  $\rightarrow$  II, as depicted in figure 15(a). To identify this bifurcation we focus on two adjacent unit cell quadrants of the lattice. We note the absence of driven flow regions around the cylinders in Phase I (figure 15(b)) and their presence in phase II (figure 15(k), marked in pink). This flow topology change occurs in two consecutive s.pdf, passing through another hidden phase of §4.2.8 in the main text.

In the first step, we draw attention to the absence of recirculating regions in Phase I (figure 15(b)) and their presence in figure 15(d) (comprised of five saddles and four centres, marked in pink). We note that the latter flow field corresponds to the hidden Phase H. The simplest Hamiltonian form that captures this transition is  $H(x, y) = ax^3y + bxy^3 + \beta xy$  with  $ab > 0$ , which corresponds to a higher order hyperbolic reflecting umbilic bifurcation (higher order with respect to the ones shown in the main text, on account of the additional symmetry due to same curvature cylinders) [45]. Here  $\beta xy$  is the unfolding term, that controls the appearance (going from  $\beta > 0$  to  $\beta < 0$ ) of the recirculating regions and their size (figure 15(e-g)). In our lattice system, the appearance and size of these regions can be controlled by decreasing  $\delta_{AC}$ , which decreases the DC layer thickness  $\delta_{DC}$  of all the cylinders. This pulls the streamlines adjacent to the marked saddle, in four opposite directions (figure 15(c)), causing it to eventually split into five saddles and four centres (figure 15(d)). Topologically, this manifests as four counter-rotating recirculating regions, thus revealing Phase H.



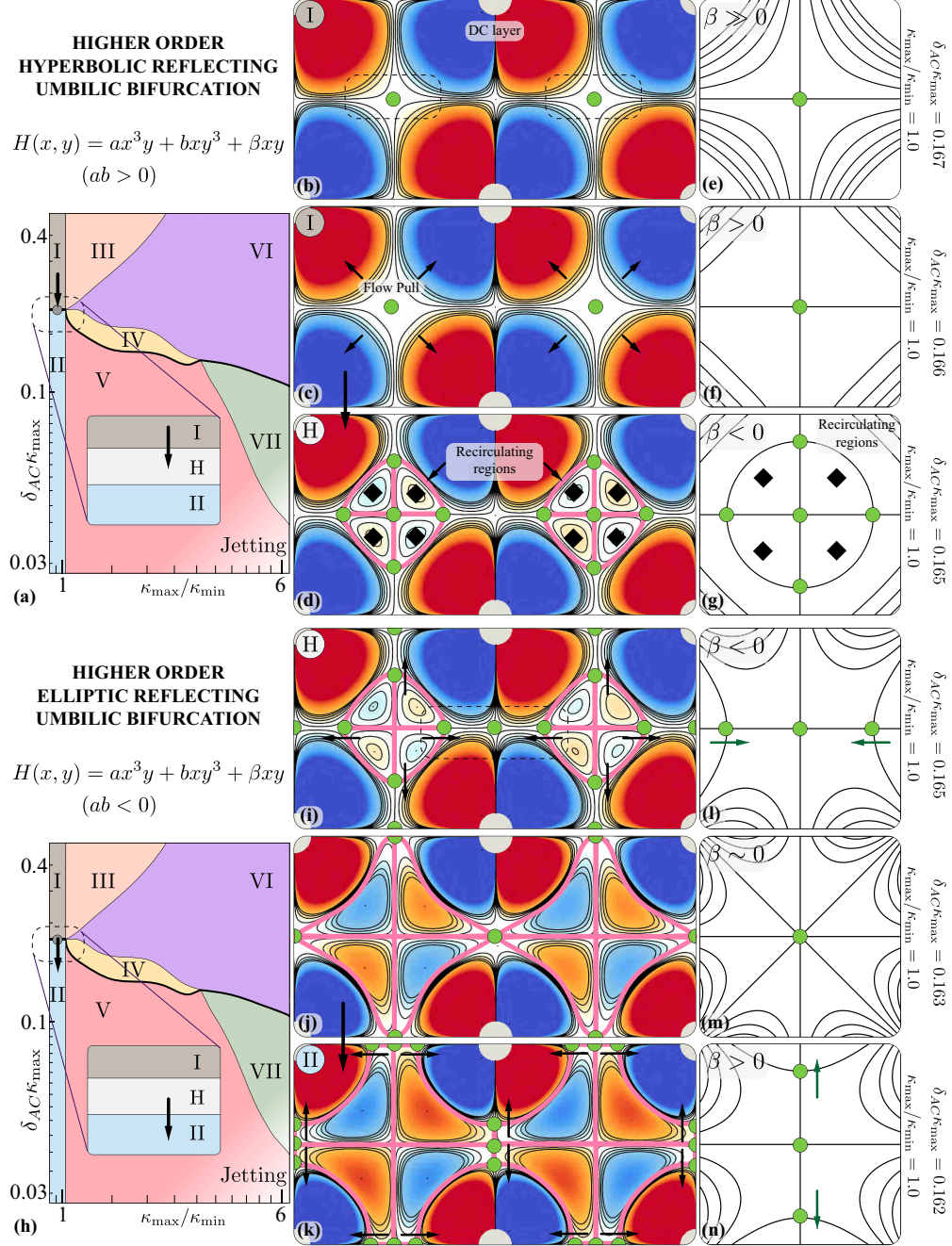


FIG. 15: Phase I  $\rightarrow$  hidden Phase H: higher order hyperbolic reflecting umbilic bifurcation. (a) The transition is highlighted on the phase space (with a zoomed in view) and the corresponding reduced Hamiltonian form is reported. (b, c, d) Flows representative of Phase I, Phase I approaching the transition, and hidden Phase H, respectively. (e, f, g) Bifurcations captured as contours of the reduced Hamiltonian form. (h) The transition from hidden Phase H  $\rightarrow$  II (higher order elliptic reflecting umbilic bifurcation) is highlighted on the phase space (with a zoomed in view) and the corresponding reduced Hamiltonian form is reported. (i, j, k) Flows representative of hidden Phase H, at the transition, and Phase II, respectively. (l, m, n) Bifurcations captured as contours of the reduced Hamiltonian form. The newly created recirculating region pairs are marked in pink.

The second step of the Phase I  $\rightarrow$  II transition occurs upon further decreasing  $\delta_{AC}$ , immediately after the previous bifurcation, thus rendering the hidden Phase H very narrow. We focus on the

saddles in the highlighted region of the unit cell, in the hidden Phase H (figure 15(i)). After the transition these saddles are located on the vertical axis passing through the highlighted region, thus recovering Phase VII (figure 15(k)). The simplest Hamiltonian form that captures this rearrangement is  $H(x, y) = ax^3y + bxy^3 + \beta xy$  with  $ab < 0$ , which corresponds to a higher order elliptic reflecting umbilic bifurcation [45]. Here  $\beta xy$  is the unfolding term, that captures whether the saddles are present ( $\beta < 0$ ) or absent ( $\beta > 0$ ) on the horizontal axis (figure 15(l-n)), as well as their distance. Similar to the previous step, a decrease in  $\delta_{AC}$  (i.e  $\delta_{DC} \downarrow$ ) causes a pull on the streamlines immediately adjacent to the cylinder's DC layers. This time though, the saddles created in the previous step are now pushed towards the saddle on the vertical axis in the highlighted region, extending the recirculating region pairs. Upon reaching the saddle on the vertical axis, the two opposite saddles collapse (figure 15(j)) and split along the vertical axis (figure 15(k)). We note that this bifurcation is observed along all the edges of the unit cell. These new saddles completely define the driven flow regions around the cylinders, thus recovering Phase II.

### C. Generalization to individual streaming bodies: additional examples

Here we provide a number of additional examples which demonstrate that our intuition from the phase space carries on to various streaming geometries and oscillatory background flow conditions. All subsequent studies entail a single shape immersed in an unbounded domain.

#### 1. Comparison against experiments: streaming triangles and diamonds

Expanding on the examples of the main text, we further test our understanding against a different set of experiments. We consider an oscillating diamond cylinder (of side  $2a$ ) [12] and a horizontally oriented triangle cylinder (of side  $2a$ ) [13].

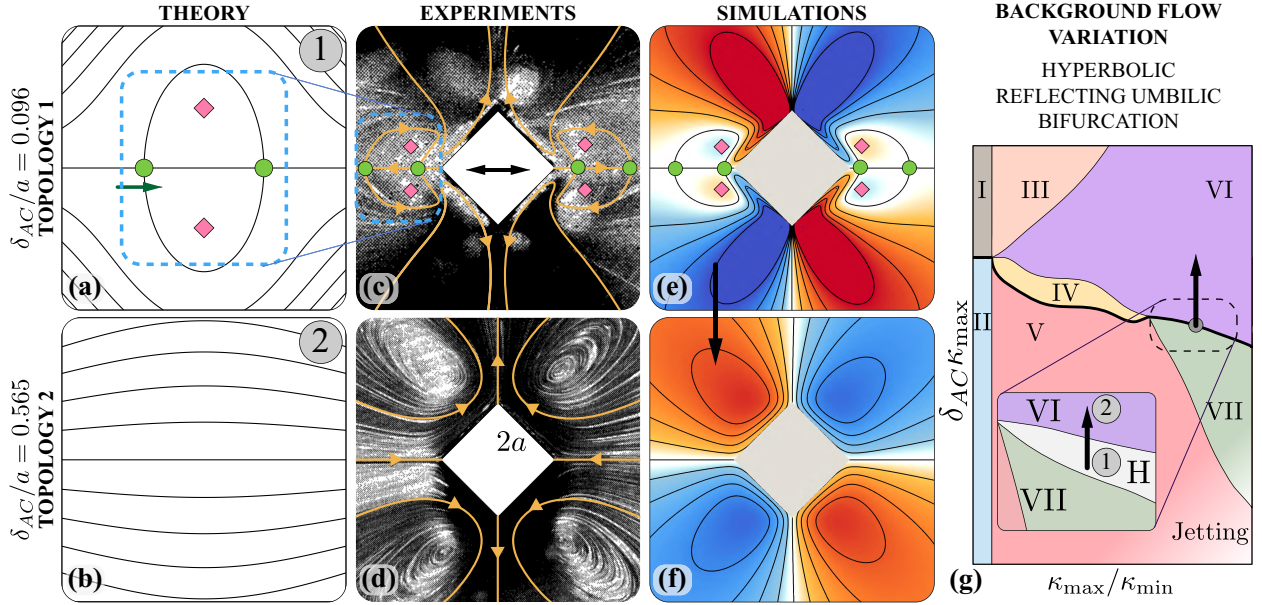


FIG. 16: Background flow variation for a diamond cylinder. (a, b) Reduced Hamiltonian form contours for hyperbolic reflecting umbilic bifurcation, associated with the transition hidden Phase H  $\rightarrow$  Phase VI in the lattice phase space. A topologically equivalent transition is observed on increasing  $\delta_{AC}/a$ , both in experiments (c, d) and simulations (e, f). (g) Mapping of the observed transition on the lattice phase space.

Figure 16 illustrates the hyperbolic reflecting umbilic bifurcation for a diamond cylinder, observed on increasing  $\delta_{AC}/a$  from 0.096 to 0.565, similar to the one observed in the lattice phase

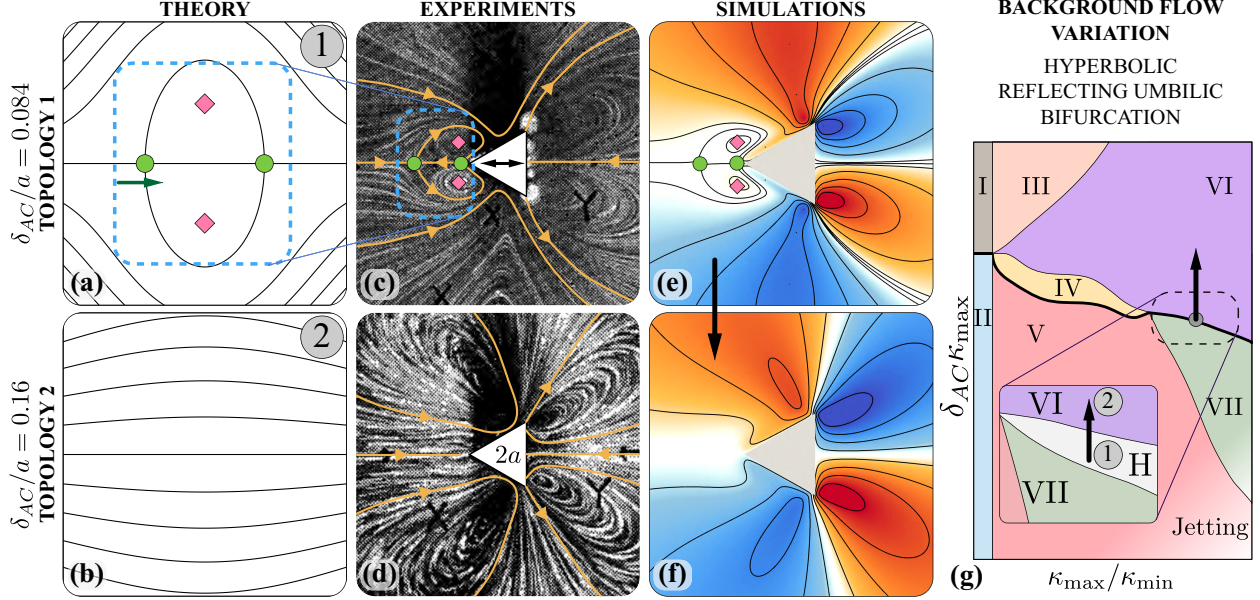


FIG. 17: Background flow variation for a horizontally oriented equilateral triangle cylinder. (a, b) Reduced Hamiltonian form contours for hyperbolic reflecting umbilic bifurcation, associated with the transition hidden Phase H  $\rightarrow$  Phase VI in the lattice phase space. A topologically equivalent transition is observed on increasing  $\delta_{AC}/a$ , both in experiments (c, d) and simulations (e, f). (g) Mapping of the observed transition on the lattice phase space.

space. Figure 16(a, b) illustrates the predicted flow topology change based on the reduced Hamiltonian contours, with confirmations against flow topologies observed in experiments (figure 16(c, d)) and simulations (figure 16(e, f)).

Figure 17 illustrates the hyperbolic reflecting umbilic bifurcation for the triangle cylinder, observed on increasing  $\delta_{AC}/a$  from 0.084 to 0.16, similar to the one observed in the lattice phase space. Once again experiments (figure 17(c, d)) and simulations (figure 17(e, f)) confirm our predictions.

## 2. Shape parametrization

Figure 18 illustrates the parameterization for the complex convex shapes, investigated in §5.2 of the main text and in §C 3 of the appendix. Figure 18(a) presents the parametrization for the hybrid circular–square bullet of figure 12(a) in the main text. This hybrid cylinder presents top-down asymmetry—the top side is a circle with constant curvature  $\kappa_0$ , while the bottom is a square with rounded corners of constant curvature  $\kappa_v$ . As  $\kappa_v$  is varied from  $\kappa_0$  to higher values ( $\rightarrow \infty$ ), the shape morphs from a circle to a circle–square hybrid with increasingly sharper corners. Figure 18(b) presents the parametrization for the hybrid circular–elliptic cylinder, which we use to demonstrate additional examples of flow topology design in the following sections. This hybrid cylinder presents left-right asymmetry—the right side is a circle with constant curvature  $\kappa_0$ , while the left side is an ellipse of aspect ratio AR (defined as height/breadth, where height is kept constant). As AR is varied from 1 to higher values, the shape morphs from a circle to a circular–elliptic cylinder with a higher AR elliptic side (with corresponding higher curvature at the corners).

## 3. Manipulation of streaming flow topology: circle to a circle–ellipse

Figure 19(a) illustrates the morphing from a circular cylinder of uniform aspect ratio (AR = 1, defined as height/breadth) to a body with a circular side having the same curvature  $\kappa_0$  and an

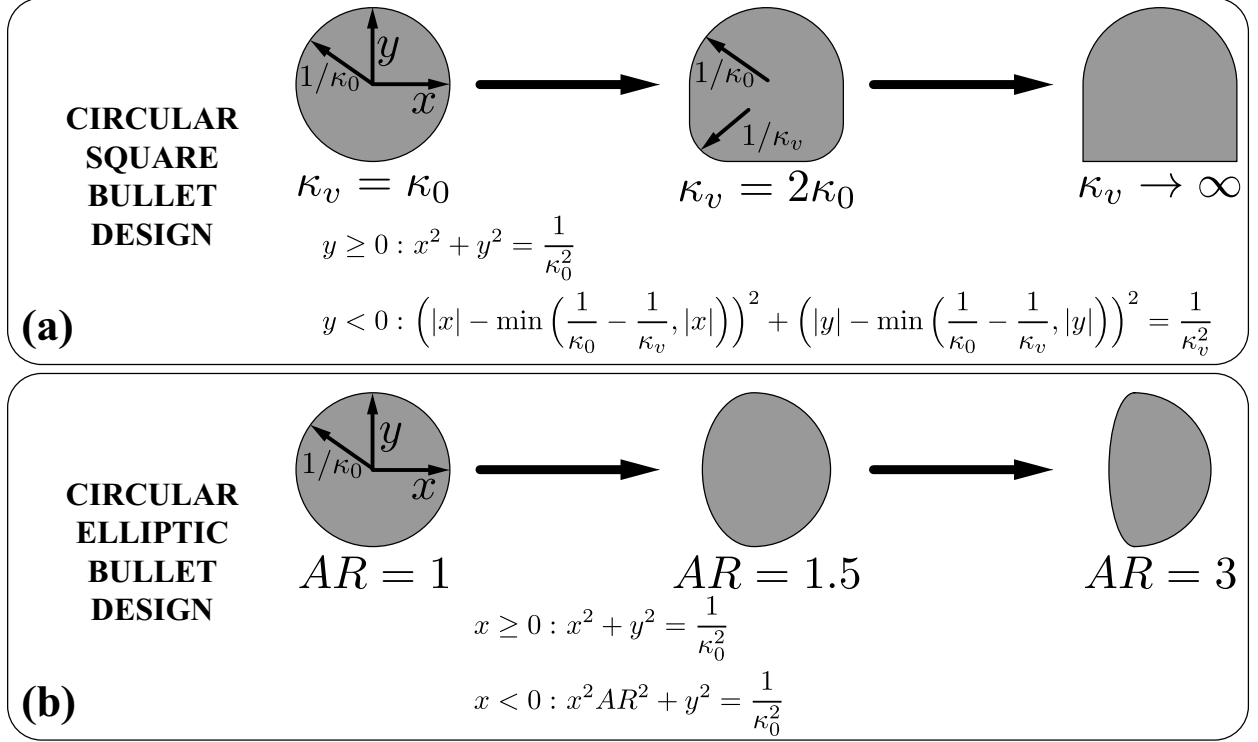


FIG. 18: Parametrization of (a) the hybrid circular-square cylinder (main text) and (b) the circular-elliptic cylinder.

elliptic side with aspect ratio  $AR > 1$ . Parametrization of this hybrid shape can be found in figure 18(b). For such  $AR$ , the body presents constant curvature  $\kappa_0$  on the circular side and a range of curvatures ( $\kappa_0/AR$  to  $AR^2\kappa_0$ ) on the elliptic side, thus introducing curvature variation in a regulated fashion.

We start by choosing a  $\delta_{AC}\kappa_{\max}$  for which the streaming flow topology for a circular cylinder ( $AR = 1$ ) lies in the finite thickness DC layer regime (figure 19(d)). We focus on the heteroclinic orbits highlighted in figure 19(d). Recalling our observations from the lattice system, we predict that introducing fore-aft shape asymmetry will lead to the breaking of these orbits, as captured by the heteroclinic orbit bifurcation from Phase II  $\rightarrow$  V (figure 19(b, c)) in the main text. Indeed, testing a shape with curvature asymmetry (i.e.  $AR > 1$ ) confirms this prediction, as seen from the flow topology in figure 19(e).

After testing our understanding against the effects of breaking symmetry, we analyse how flow topology evolves on further increase in curvature variation (i.e. increase in  $AR$ ) for the body. Figure 20(e) depicts the streaming flow topology for the body with  $AR > 1$ , where the shape parameters and flow topology are retained from figure 19(e). We focus on the highlighted saddle (defining DC layer extent) forming the homoclinic orbit, and the centre within this orbit. As  $AR$  increases, (figure 20(a)), the local curvature on the body near the saddle increases. Based on the transitions  $V \rightarrow VII$  and  $III \rightarrow VI$  associated with such a curvature increase in the lattice phase space, we predict that this will lead to a decrease in the saddle-centre distance, while shrinking the corresponding homoclinic orbit. Then beyond a critical value of  $AR$  the orbit will eventually disappear through a saddle-centre annihilation, similar to the bifurcation seen from Phase V  $\rightarrow$  VII. Figure 20(b, c, d) demonstrate the reduced Hamiltonian form contours for this system and showcase the saddle-centre bifurcation. Indeed, testing a shape with curvature variation (higher  $AR$ ) confirms these predictions, as seen from the flow topologies in figure 20(f, g).



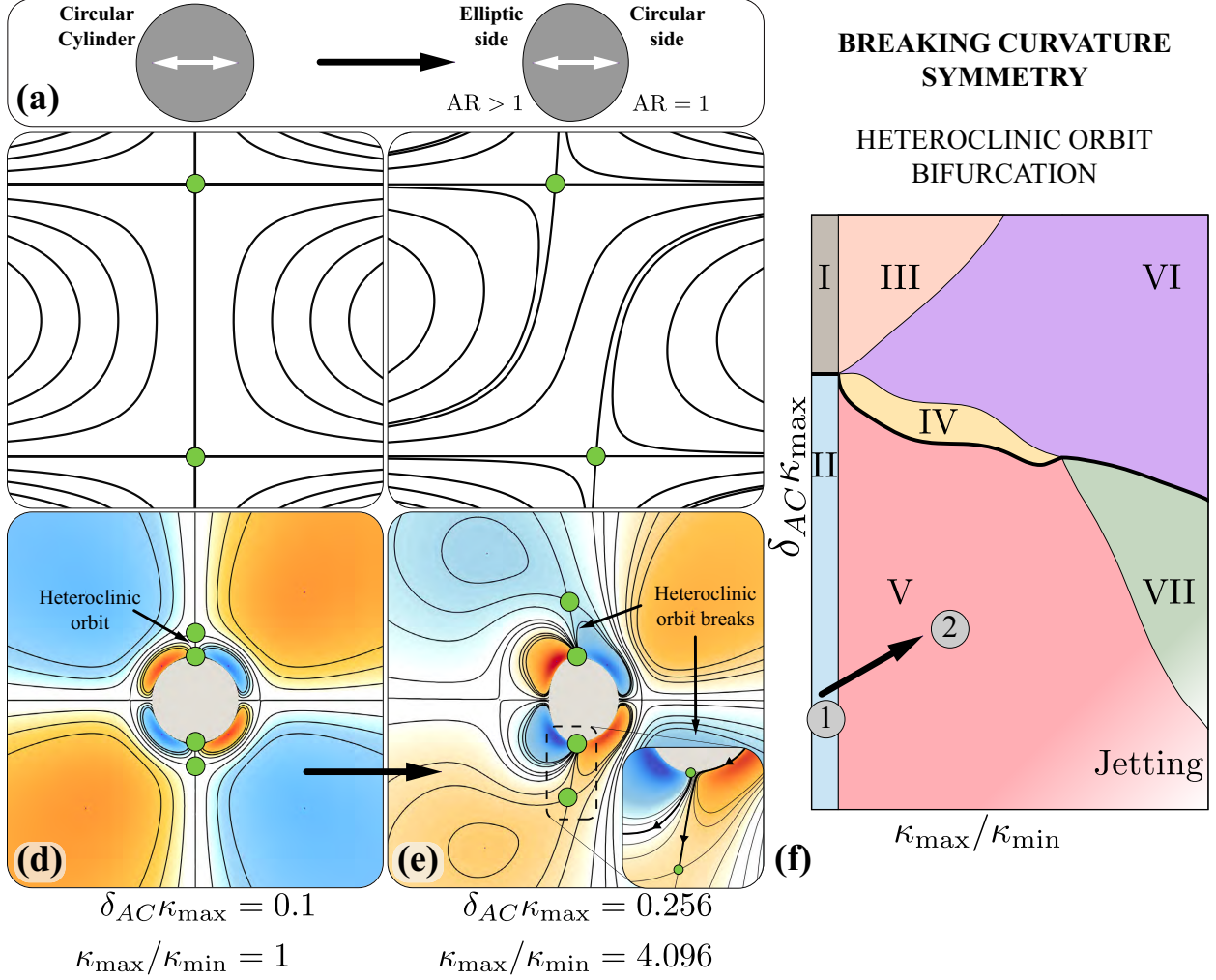


FIG. 19: Breaking symmetry. (a) Illustration of morphing a circular cylinder into a hybrid circular–elliptic cylinder with a circular side and an elliptic side with varying aspect ratio (AR). (b, c) present the reduced Hamiltonian form contours for heteroclinic orbit bifurcation, associated with the transition  $\text{II} \rightarrow \text{V}$  in the lattice phase space. The morphed body presents a topologically equivalent transition on breaking symmetry, presented in (d, e). (f) Mapping of the observed transition on the lattice phase space.

For completion, figure 21 presents a step-by-step systematic variation of geometric and background flow properties for the morphing from a circular cylinder to a hybrid circular–elliptic cylinder. We observe a wide range of flow topologies, which are predicted (reduced Hamiltonian as grey contours) by drawing intuition from the transitions observed in the lattice phase space with corresponding confirmations from simulations. We note that the same set of bifurcations as that of the circular–square cylinder in the main text, are encountered for the circular–elliptic cylinder. Figure 21(b, c) illustrate the heteroclinic orbit bifurcation (prediction and confirmation), observed on breaking symmetry described above. Figure 21(c, d) illustrate the saddle–centre bifurcation (prediction and confirmation), observed on curvature variation described above. Figure 21(d, e) and figure 21(e, f) illustrate the elliptic reflecting umbilic bifurcation and the hyperbolic reflecting umbilic bifurcation, respectively, observed on increasing  $\delta_{AC}$  in the lattice phase space, with the predicted flow topology change based on the reduced Hamiltonian contours and confirmations against flow topologies observed in simulations.

In summary, this section illustrates an additional example of how our approach can be employed

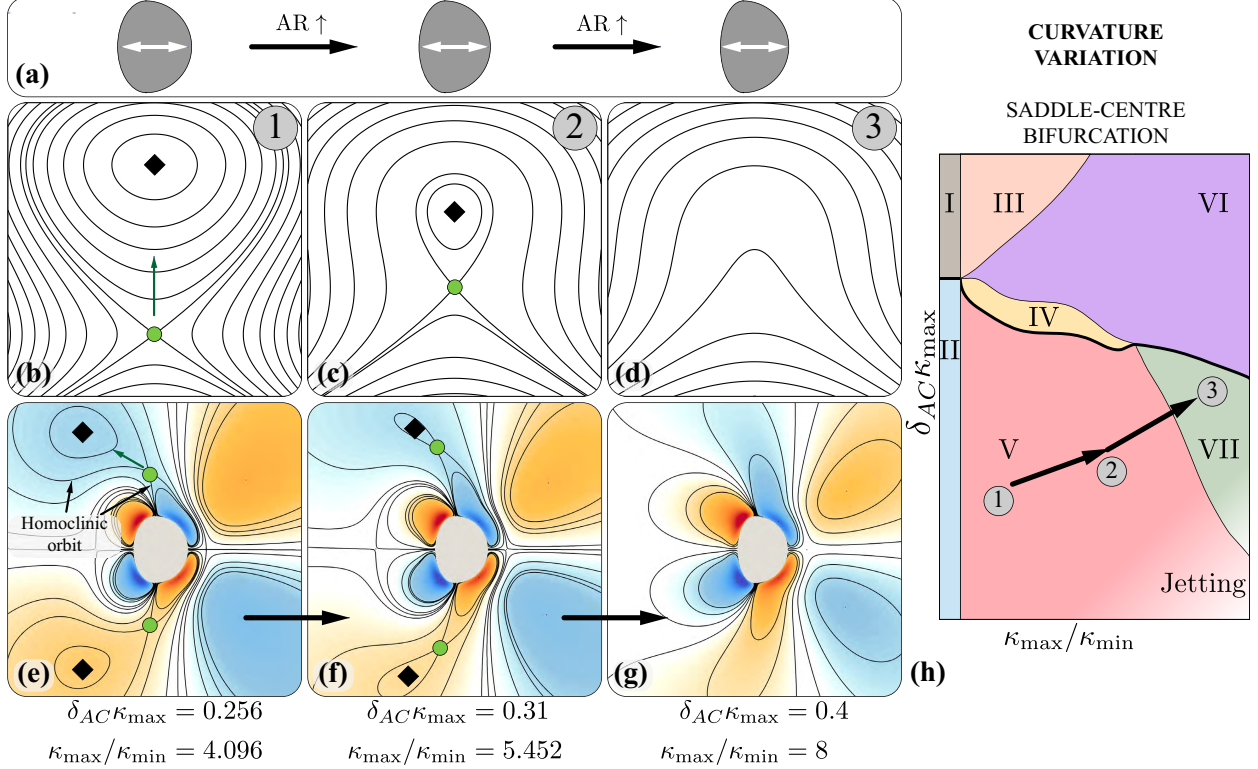


FIG. 20: Varying curvature ratio. (a) Illustration of increasing curvature variation (increasing AR) for the circular-elliptic hybrid. (b, c, d) present the reduced Hamiltonian form contours for saddle-centre bifurcation, similar to the supercritical pitchfork bifurcation, associated with the transition  $V \rightarrow VII$  in the lattice phase space. A topologically equivalent transition is observed on morphing the body, presented in (e, f, g). (h) Mapping of the observed transition on the lattice phase space.

to predict and design streaming flow topologies, in a rational fashion.

#### 4. Varying ellipse aspect ratio

Figure 22(a) illustrates the use of our phase space in the case of ellipses of varying aspect ratio (defined as height/breadth). We keep the major axis (height =  $L$ ) fixed. This allows us to introduce curvature variation in a regulated fashion by spanning AR. We start by choosing a  $\delta_{AC}\kappa_{\max}$  and AR for which the streaming flow topology for the ellipse lies in the finite thickness DC layer regime (figure 22(b)). We note that a mapping of this local flow topology to Phase I and II of our lattice system is not possible due to the variation of curvature on an ellipse (Phase I and II necessitate constant curvature). Additionally, mapping to Phases III, IV and V does not exist as we do not break fore-aft or top-down shape symmetry when we vary AR for an ellipse (figure 22(a)). This means that we don't break symmetry for the DC layer bounding heteroclinic orbits which are necessary for Phases III, IV and V to exist.

We focus on the highlighted saddles bounding the DC layers on the vertical axis, near the top and bottom ends of the ellipse. These structures closely resemble Phase VII of figure 7( $k, n$ ) in the main text, where the second saddle (not imaged in experiments) is located at infinity. Thus, as  $\delta_{AC}\kappa_{\max}$  increases (on increasing AR), we predict that the saddles will progressively move outwards, to approach the saddles at infinity and undergo an elliptic reflecting umbilic bifurcation. This has the overall effect to “open up” the DC layers on the vertical axis of the ellipse. Additionally, we note that the highlighted flow structures on the left/right of the streaming shape can be mapped

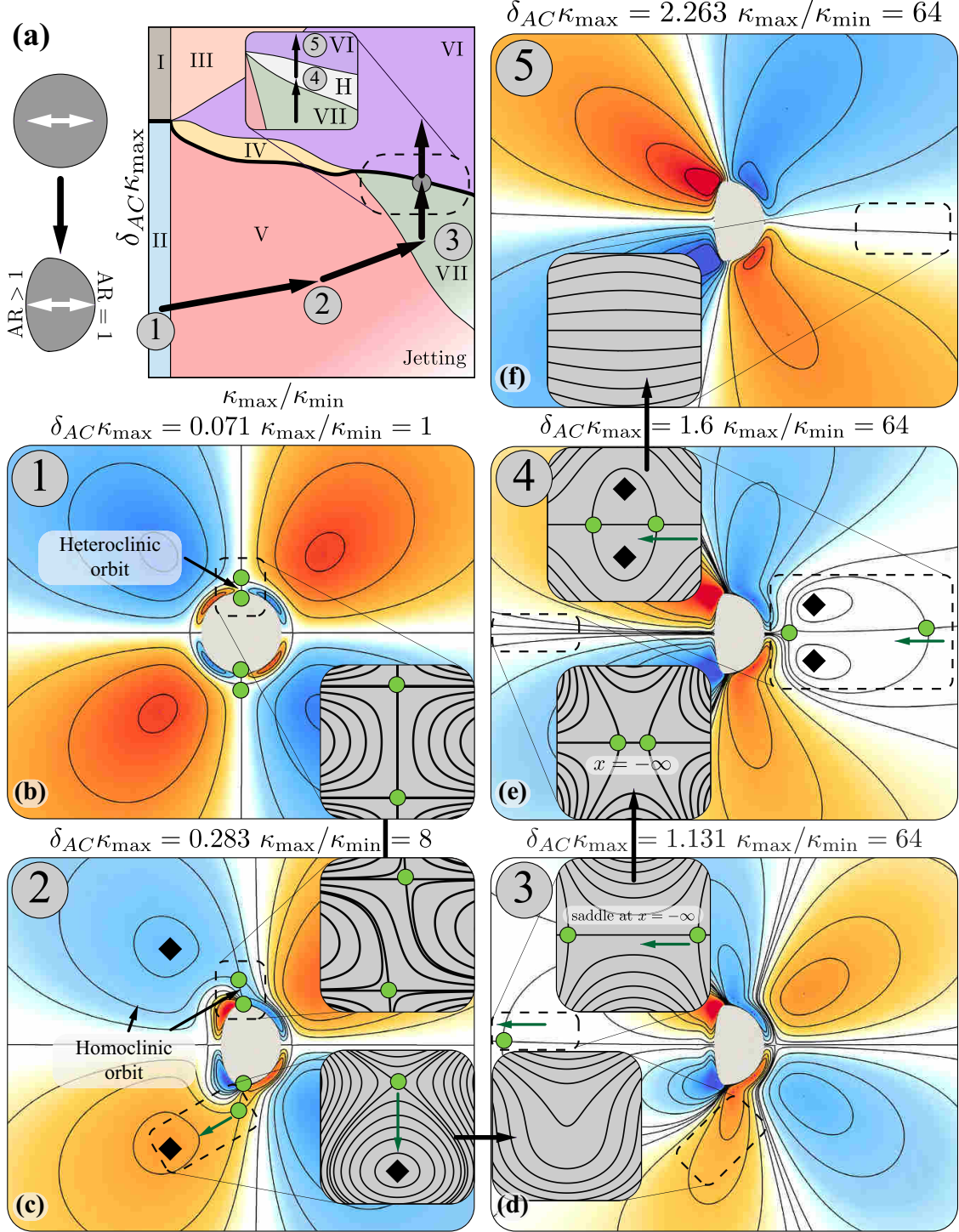


FIG. 21: Flow topology manipulation. (a) Illustration of morphing a circular cylinder into a hybrid circular–elliptic cylinder. Mapping of the observed transitions on the lattice phase space. (b–f) present the different topologies observed on geometric and background flow variation, with the concerned critical points highlighted and the predictions (reduced Hamiltonian form contours) illustrated as grey contours.

to Phase H of figure 7(d, g) (with one saddle at infinity). Therefore, as a side effect of the increase in  $\delta_{AC}\kappa_{\max}$ , we predict that the saddles at infinity enter the imaged domain and form closed

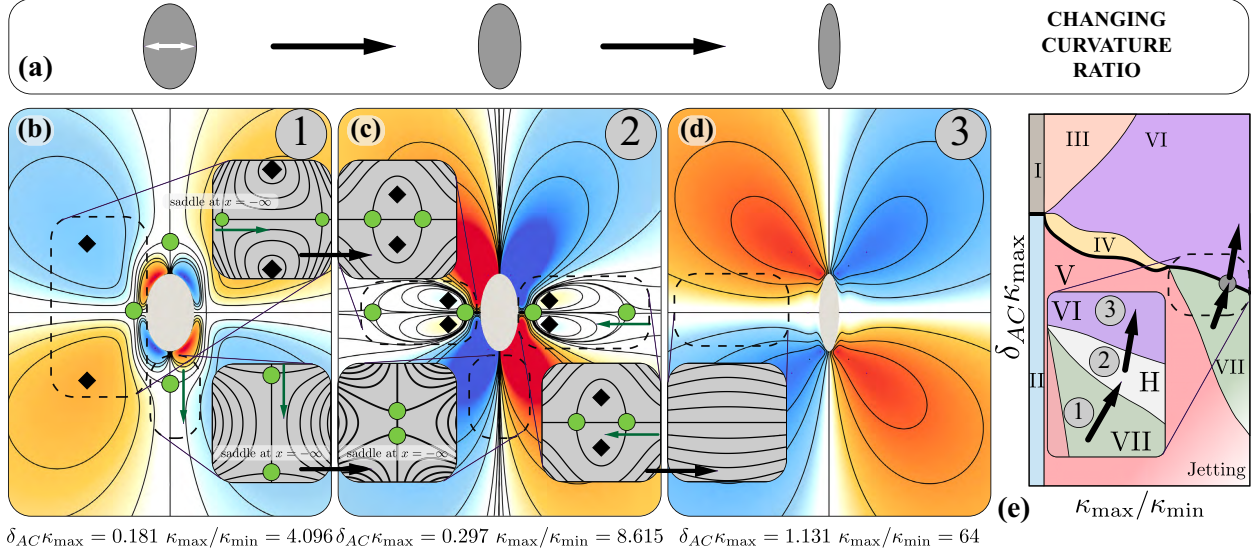


FIG. 22: Flow topology manipulation. (a) Illustration of varying curvature of an ellipse by varying the aspect ratio AR. (b-d) present the different topologies observed on geometric variation, with the concerned critical points highlighted and the predictions (reduced Hamiltonian form contours) illustrated as grey contours. (e) Mapping of the observed transitions on the lattice phase space.

recirculating regions on the left and right side of the ellipse. Computations of figure 22(c) confirm this intuition.

We then focus on the highlighted saddles and centres forming recirculating regions on the horizontal axis of the ellipse in figure 22(c). These structures closely resemble the hidden Phase H of figure 7(d, g). Based on our phase space, we predict that as  $\delta_{AC}\kappa_{\max}$  increases (on increasing AR), the system will transition to a new topology corresponding to Phase VI, via a hyperbolic reflecting umbilic bifurcation. This is a consequence of the saddles and centres moving closer and closer, eventually collapsing and vanishing. Once again, computations of figure 22(d) confirm this intuition.

We note that in the ellipse case, due to its geometrical properties, some phases captured in our lattice phase space do not exist (see above discussion). Nonetheless, the phases and the transitions that do exist remain consistent with the lattice phase space, and so our analysis is still valid.

- 
- [1] J Holtmark, I Johnsen, To Sikkeland, and S Skavlem. Boundary layer flow near a cylindrical obstacle in an oscillating, incompressible fluid. *The Journal of the Acoustical Society of America*, 26(1):26–39, 1954.
  - [2] Norman Riley. Steady streaming. *Annual Review of Fluid Mechanics*, 33(1):43–65, 2001.
  - [3] Barry R Lutz, Jian Chen, and Daniel T Schwartz. Microscopic steady streaming eddies created around short cylinders in a channel: Flow visualization and stokes layer scaling. *Physics of Fluids*, 17(2): 023601, 2005.
  - [4] W Coenen. Oscillatory flow about a cylinder pair with unequal radii. *Fluid Dynamics Research*, 45(5): 055511, 2013.
  - [5] Giridar Vishwanathan and Gabriel Juarez. Steady streaming flows in viscoelastic liquids. *arXiv preprint arXiv:1903.02609*, 2019.
  - [6] MB Glauert. The laminar boundary layer on oscillating plates and cylinders. *Journal of Fluid Mechanics*, 1(1):97–110, 1956.
  - [7] Akira Yoshizawa. Steady streaming induced by an oscillating flat plate in a viscous fluid. *Journal of*



- the Physical Society of Japan*, 37(2):524–528, 1974.
- [8] CA Lane. Acoustical streaming in the vicinity of a sphere. *The Journal of the Acoustical Society of America*, 27(6):1082–1086, 1955.
  - [9] N Riley. On a sphere oscillating in a viscous fluid. *The Quarterly Journal of Mechanics and Applied Mathematics*, 19(4):461–472, 1966.
  - [10] C.W. Kotas, M. Yoda, and P.H. Rogers. Visualization of steady streaming near oscillating spheroids. *Experiments in Fluids*, 42(1):111–121, 2007.
  - [11] HM Badr. Oscillating viscous flow over an inclined elliptic cylinder. *Ocean Engineering*, 21(4):401–426, 1994.
  - [12] Masakazu Tatsuno. Circulatory streaming in the vicinity of an oscillating square cylinder. *Journal of the Physical Society of Japan*, 36(4):1185–1191, 1974.
  - [13] Masakazu Tatsuno. Circulatory streaming in the vicinity of an oscillating triangular cylinder. *Journal of the Physical Society of Japan*, 38(1):257–264, 1975.
  - [14] Nitesh Nama, Po-Hsun Huang, Tony Jun Huang, and Francesco Costanzo. Investigation of acoustic streaming patterns around oscillating sharp edges. *Lab on a Chip*, 14(15):2824–2836, 2014.
  - [15] Mikhail Ovchinnikov, Jianbo Zhou, and Satish Yalamanchili. Acoustic streaming of a sharp edge. *The Journal of the Acoustical Society of America*, 136(1):22–29, 2014.
  - [16] B Yan, DB Ingham, and BR Morton. The streaming flow initiated by oscillating cascades of cylinders and their stability. *Physics of Fluids*, 6(4):1472–1481, 1994.
  - [17] W Coenen. Steady streaming around a cylinder pair. *Proceedings of the Royal Society A: Mathematical, Physical and Engineering Sciences*, 472(2195):20160522, 2016.
  - [18] Robin H Liu, Jianing Yang, Maciej Z Pindera, Mahesh Athavale, and Piotr Grodzinski. Bubble-induced acoustic micromixing. *Lab on a Chip*, 2(3):151–157, 2002.
  - [19] Barry R Lutz, Jian Chen, and Daniel T Schwartz. Microfluidics without microfabrication. *Proceedings of the National Academy of Sciences*, 100(8):4395–4398, 2003.
  - [20] Philippe Marmottant and Sascha Hilgenfeldt. A bubble-driven microfluidic transport element for bio-engineering. *Proceedings of the National Academy of Sciences*, 101(26):9523–9527, 2004.
  - [21] Sujit Nair and Eva Kanso. Hydrodynamically coupled rigid bodies. *Journal of Fluid Mechanics*, 592:393–411, 2007.
  - [22] Sang Kug Chung and Sung Kwon Cho. 3-d manipulation of millimeter-and micro-sized objects using an acoustically excited oscillating bubble. *Microfluidics and Nanofluidics*, 6(2):261–265, 2009.
  - [23] AA Tchieu, D Crowdy, and A Leonard. Fluid-structure interaction of two bodies in an inviscid fluid. *Physics of Fluids*, 22(10):107101, 2010.
  - [24] Cheng Wang, Shreyas V Jalikop, and Sascha Hilgenfeldt. Size-sensitive sorting of microparticles through control of flow geometry. *Applied Physics Letters*, 99(3):034101, 2011.
  - [25] Kwitae Chong, Scott D Kelly, Stuart Smith, and Jeff D Eldredge. Inertial particle trapping in viscous streaming. *Physics of Fluids*, 25(3):033602, 2013.
  - [26] Daphne Klotz, Kyle A Baldwin, Richard JA Hill, Roger M Bowley, and Michael R Swift. Propulsion of a two-sphere swimmer. *Physical Review Letters*, 115(24):248102, 2015.
  - [27] Raqeeb Thameem, Bhargav Rallabandi, and Sascha Hilgenfeldt. Particle migration and sorting in microbubble streaming flows. *Biomicrofluidics*, 10(1):014124, 2016.
  - [28] Raqeeb Thameem, Bhargav Rallabandi, and Sascha Hilgenfeldt. Fast inertial particle manipulation in oscillating flows. *Physical Review Fluids*, 2(5):052001, 2017.
  - [29] Brian J Williams, Sandeep V Anand, Jagannathan Rajagopalan, and M Taher A Saif. A self-propelled biohybrid swimmer at low reynolds number. *Nature Communications*, 5:3081, 2014.
  - [30] Sung-Jin Park, Mattia Gazzola, Kyung Soo Park, Shirley Park, Valentina Di Santo, Erin L Blevins, Johan U Lind, Patrick H Campbell, Stephanie Dauth, Andrew K Capulli, et al. Phototactic guidance of a tissue-engineered soft-robotic ray. *Science*, 353(6295):158–162, 2016.
  - [31] Hakan Ceylan, Joshua Giltinan, Kristen Kozielski, and Metin Sitti. Mobile microrobots for bioengineering applications. *Lab on a Chip*, 17(10):1705–1724, 2017.
  - [32] Onur Aydin, Xiaotian Zhang, Sittinon Nuethong, Gelson J Pagan-Diaz, Rashid Bashir, Mattia Gazzola, and M Taher A Saif. Neuromuscular actuation of biohybrid motile bots. *Proceedings of the National Academy of Sciences*, page 201907051, 2019.
  - [33] H-W Huang, Fazil Emre Uslu, Panayiota Katsamba, Eric Lauga, MS Sakar, and BJ Nelson. Adaptive locomotion of artificial microswimmers. *Science Advances*, 5(1):eaau1532, 2019.

- [34] Tejaswin Parthasarathy, Fan Kiat Chan, and Mattia Gazzola. Streaming-enhanced flow-mediated transport. *Journal of Fluid Mechanics*, 878:647–662, 2019.
- [35] M. Gazzola, P. Chatelain, W.M. van Rees, and P. Koumoutsakos. Simulations of single and multiple swimmers with non-divergence free deforming geometries. *Journal of Computational Physics*, 230(19): 7093–7114, 2011. doi: 10.1016/j.jcp.2011.04.025.
- [36] Mattia Gazzola, Chloe Mimeau, Andrew A Tchieu, and Petros Koumoutsakos. Flow mediated interactions between two cylinders at finite re numbers. *Physics of fluids*, 24(4):043103, 2012.
- [37] Mattia Gazzola, Wim M Van Rees, and Petros Koumoutsakos. C-start: optimal start of larval fish. *Journal of Fluid Mechanics*, 698:5–18, 2012.
- [38] Mattia Gazzola, Babak Hejazialhosseini, and Petros Koumoutsakos. Reinforcement learning and wavelet adapted vortex methods for simulations of self-propelled swimmers. *SIAM Journal on Scientific Computing*, 36(3):B622–B639, 2014.
- [39] Mattia Gazzola, Andrew A Tchieu, Dmitry Alexeev, Alexia de Brauer, and Petros Koumoutsakos. Learning to school in the presence of hydrodynamic interactions. *Journal of Fluid Mechanics*, 789: 726–749, 2016.
- [40] GK Batchelor. An introduction to fluid dynamics. *An Introduction to Fluid Dynamics, by GK Batchelor*, pp. 635. ISBN 0521663962. Cambridge, UK: Cambridge University Press, February 2000., page 635, 2000.
- [41] JT Stuart. Double boundary layers in oscillatory viscous flow. *Journal of Fluid Mechanics*, 24(4): 673–687, 1966.
- [42] A Bertelsen, Aslak Svoldal, and Sigve Tjøtta. Nonlinear streaming effects associated with oscillating cylinders. *Journal of Fluid Mechanics*, 59(3):493–511, 1973.
- [43] Anthony E Perry and Min S Chong. A description of eddying motions and flow patterns using critical-point concepts. *Annual Review of Fluid Mechanics*, 19(1):125–155, 1987.
- [44] Magnus Dam, Jens Juul Rasmussen, Volker Naulin, and Morten Brøns. Topological bifurcations in the evolution of coherent structures in a convection model. *Physics of Plasmas*, 24(8):082301, 2017.
- [45] Maikel Bosschaert and Heinz Hanßmann. Bifurcations in hamiltonian systems with a reflecting symmetry. *Qualitative Theory of Dynamical Systems*, 12(1):67–87, 2013.
- [46] Steven H Strogatz. *Nonlinear Dynamics and Chaos with Student Solutions Manual: With Applications to Physics, Biology, Chemistry, and Engineering*. CRC Press, 2018.
- [47] BJ Davidson and N Riley. Jets induced by oscillatory motion. *Journal of Fluid Mechanics*, 53(2): 287–303, 1972.
- [48] Arnold F Bertelsen. An experimental investigation of high reynolds number steady streaming generated by oscillating cylinders. *Journal of Fluid Mechanics*, 64(3):589–598, 1974.
- [49] Tejaswin Parthasarathy. Viscous streaming-enhanced inertial particle transport. Master’s thesis, 2018. URL <https://www.ideals.illinois.edu/handle/2142/102963>.
- [50] Yuri A Kuznetsov. *Elements of applied bifurcation theory*, volume 112. Springer Science & Business Media, 2013.
- [51] James Murdock. Unfoldings. *Scholarpedia*, 1(12):1904, 2006.
- [52] Pietro-Luciano Buono, Frédéric Laurent-Polz, and James Montaldi. Symmetric hamiltonian bifurcations. *Geometric Mechanics and Symmetry: the Peyresq Lectures*, pages 357–402, 2005.
- [53] John Towns, Timothy Cockerill, Maytal Dahan, Ian Foster, Kelly Gaither, Andrew Grimshaw, Victor Hazlewood, Scott Lathrop, Dave Lifka, Gregory D Peterson, et al. Xsede: accelerating scientific discovery. *Computing in Science & Engineering*, 16(5):62–74, 2014.